

EXPLORING H₂O PROMINENCE IN REFLECTION SPECTRA OF COOL GIANT PLANETS

RYAN J. MACDONALD

*Institute of Astronomy
University of Cambridge
Cambridge, CB3 0HA, UK*

MARK S. MARLEY

*NASA Ames Research Center
Moffett Field, CA 94035, USA*

JONATHAN J. FORTNEY

*University of California
1156 High Street
Santa Cruz, CA 95064, USA*

NIKOLE K. LEWIS

*Space Telescope Science Institute
3700 San Martin Drive
Baltimore, MD 21218, USA*

(Accepted March 30, 2018)

Submitted to ApJ

ABSTRACT

The H₂O abundance of a planetary atmosphere is a powerful indicator of formation conditions. Inferring H₂O in the solar system giant planets is challenging, due to condensation depleting the upper atmosphere of water vapour. Substantially warmer hot Jupiter exoplanets readily allow detections of H₂O via transmission spectroscopy, but such signatures are often diminished by the presence of clouds of other species. In contrast, highly scattering H₂O clouds can brighten planets in reflected light, enhancing molecular signatures. Here, we present an extensive parameter space survey of the prominence of H₂O absorption features in reflection spectra of cool ($T_{\text{eff}} < 400\text{K}$) giant exoplanetary atmospheres. The impact of effective temperature, gravity, metallicity, and sedimentation efficiency is explored. We find prominent H₂O features around $0.94\ \mu\text{m}$, $0.83\ \mu\text{m}$, and across a wide spectral region from $0.4\text{--}0.73\ \mu\text{m}$. The $0.94\ \mu\text{m}$ feature is only detectable where high-altitude water clouds brighten the planet: $T_{\text{eff}} \sim 150\ \text{K}$, $g \gtrsim 20\ \text{ms}^{-2}$, $f_{\text{sed}} \gtrsim 3$, $m \lesssim 10\times$ solar. In contrast, planets with $g \lesssim 20\ \text{ms}^{-2}$ and $T_{\text{eff}} \gtrsim 180\ \text{K}$ display substantially prominent H₂O features embedded in the Rayleigh scattering slope from $0.4\text{--}0.73\ \mu\text{m}$ over a wide parameter space. High f_{sed} enhances H₂O features around $0.94\ \mu\text{m}$, and enables these features to be detected at lower temperatures. High m results in dampened H₂O absorption features, due to H₂O vapour condensing to form bright optically thick clouds that dominate the continuum. We verify these trends via self-consistent modelling of the low gravity exoplanet HD 192310c, revealing that its reflection spectrum is expected to be dominated by H₂O absorption from $0.4\text{--}0.73\ \mu\text{m}$ for $m \lesssim 10\times$ solar. Our results demonstrate that H₂O is manifestly detectable in reflected light spectra of cool giant planets only marginally warmer than Jupiter, providing an avenue to directly constrain the C/O and O/H ratios of a hitherto unexplored population of exoplanetary atmospheres.

Keywords: planets and satellites: atmospheres

1. INTRODUCTION

Spectroscopy of exoplanetary atmospheres has opened a new frontier in planetary science. The combined efforts of space-based and ground-based telescopes have resulted in conclusive detections of H₂O, CH₄, CO, TiO, Na, and K (e.g Deming et al. 2013; Macintosh et al. 2015; Snellen et al. 2010; Sedaghati et al. 2017; Snellen et al. 2008; Wilson et al. 2015), along with evidence of species such as VO, HCN, and NH₃ (e.g Evans et al. 2017; MacDonald & Madhusudhan 2017). Extracting abundances of these trace species from spectroscopic observations has been made possible by atmospheric retrieval techniques for exoplanets (e.g Madhusudhan & Seager 2009; Line et al. 2013; Lupu et al. 2016). The abundance of H₂O, in particular, has received intense attention as a potential diagnostic of planetary formation mechanisms (Öberg et al. 2011; van Dishoeck et al. 2014).

Comparative studies of H₂O in giant planet atmospheres has been pioneered by analyses of hot Jupiters (Madhusudhan et al. 2014). The high temperatures of these worlds ($\sim 1000\text{--}3000$ K) renders H₂O into vapour form throughout the atmosphere, resulting in strong infrared absorption features routinely observed in transmission and emission spectra (Kreidberg et al. 2014b; Sing et al. 2016). More recently, detections of H₂O have been extended to cooler exo-Neptunes (~ 1000 K) (Fraine et al. 2014; Wakeford et al. 2017) and thermally bright directly imaged planets in the outermost regions of young stars (~ 1000 K) (Konopacky et al. 2013; Barman et al. 2015). At cooler temperatures, such as those of the solar system giant planets (~ 100 K), H₂O condenses deep in the atmosphere, depleting their upper atmospheres of detectable quantities of H₂O vapour (Atreya et al. 1999).

Most H₂O absorption features observed via transmission spectroscopy are lower-amplitude than expected of a solar-composition cloud-free atmosphere (Sing et al. 2016). Such diminished features could be caused by a low atmospheric O abundance (Madhusudhan et al. 2014), or by obscuration due to high altitude clouds or hazes (Deming et al. 2013). Due to the slant geometry during primary transit, even a relatively vertically-thin cloud deck can result in large optical depths (Fortney 2005). In extreme cases, such obscuration can result in characteristically flat transmission spectra devoid of spectral features (Ehrenreich et al. 2014; Knutson et al. 2014; Kreidberg et al. 2014a). Where low-amplitude H₂O features are detected, the possibility of clouds can incur additional degeneracies when retrieving transmission spectra, resulting in weaker abundance constraints (Benneke 2015).

Reflection spectroscopy offers an alternative route to characterise exoplanetary atmospheres. Contrasting with transmission spectra, early theoretical studies predicted that clouds can enhance molecular absorption features observed in reflected light (Marley et al. 1999; Sudarsky et al. 2000; Burrows et al. 2004; Sudarsky et al. 2005). This enhance-

ment is caused by backscattering of photons from highly reflective clouds, enabling light that would otherwise have been consumed in the deep atmosphere to instead reach the observer. The resulting effect is an overall brightening of the planet and the accrual of absorption features from backscattered photons traversing the observable atmosphere.

Reflection spectra of Jupiter do not reveal signatures of H₂O (Karkoschka 1998). At such low temperatures ($T_{\text{eff}} \sim 100$ K) both NH₃ and H₂O clouds form, with the H₂O clouds sufficiently deep (~ 5 bar) as to render the observable upper atmosphere depleted of H₂O vapour. In-situ constraints on the Jovian H₂O abundance from the Galileo entry probe reported a value of $0.3\times$ solar, contrasting with $2\text{--}3\times$ solar measured for C, N, S, Ar, Kr, and Xe (Wong et al. 2004). This is surprising, as core accretion formation models assuming a solar-composition nebula predict an enhanced H₂O abundance of $3\text{--}7\times$ solar (Mousis et al. 2012). Resolving the question of the global Jovian O abundance is one of the key science goals of NASA’s Juno mission (Bolton 2010).

Cool giant planets marginally warmer than Jupiter are expected to display signatures of H₂O in reflected light. Early studies noted that exoplanets with $T_{\text{eff}} \sim 200$ K possess reflection spectra showing H₂O absorption at $0.94\ \mu\text{m}$ (Marley et al. 1999; Sudarsky et al. 2000; Burrows et al. 2004). More recent studies confirmed that H₂O signatures are apparent for semi-major axes < 5 AU (Cahoy et al. 2010) and for thin, sufficiently deep, water clouds (Morley et al. 2015). Burrows (2014) additionally noted that such H₂O signatures could serve as a diagnostic for metallicity. However, there has yet to be a thorough investigation of the prominence of H₂O signatures in cool giant planet reflection spectra across a wide range of planetary properties. Identifying regions of parameter space with detectable H₂O informs future direct imaging missions, such as WFIRST (Spergel et al. 2015), LUVOIR (Bolcar et al. 2016), HabEx (Mennesson et al. 2016), and similar concepts. Direct imaging spectroscopy in this manner will constrain the O abundances of an unexplored population of exoplanetary atmospheres, providing new insights into the formation of cool giant planets.

In this study, we present an extensive parameter space survey of the prominence of H₂O in reflection spectra of cool giant planets. We explore the influence of a wide range of effective temperatures, gravities, metallicities, and sedimentation efficiencies, providing a grid of $> 50,000$ models for the community. In what follows, we espouse the principal components of reflection spectra models in §2. We illustrate how H₂O signatures are influenced by planetary parameters in §3. We identify how to maximise the detectability of H₂O signatures in cool giant planets in §4. The implications for observations and promising target planets for direct imaging spectroscopy are presented in §5. Finally, in §6, we summarise our results and discuss wider implications.

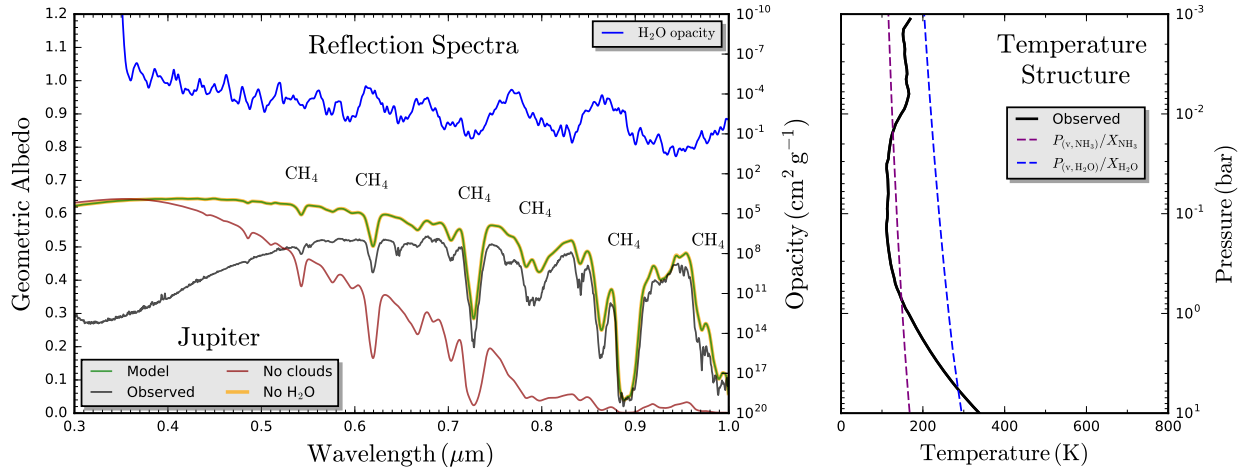


Figure 1. Jovian geometric albedo spectra and temperature structure. Left: comparison of reflection spectra models including clouds (green), without clouds (red), without H₂O vapour (orange), and the observed disk-integrated spectrum of Karkoschka (1994) (black). Prominent CH₄ absorption features are annotated. The spectrum with H₂O vapour removed is identical to that with H₂O present, indicating no H₂O signatures are present for Jupiter. The H₂O opacity is shown in blue (smoothed for clarity). Right: Voyager-derived temperature structure of Jupiter (black) (Lindal et al. 1981), with the NH₃ (purple) and H₂O (blue) condensation curves for a 3× solar atmosphere.

2. REFLECTION SPECTROSCOPY OF EXOPLANETARY ATMOSPHERES

We begin with a brief exploration of reflection spectroscopy, focusing specifically on the physical processes that control their appearance. We qualitatively illustrate these features through consideration of Jupiter’s reflection spectrum, before elaborating on the computation of reflection spectra for exoplanetary atmospheres.

2.1. Geometric Albedo Spectra

Consider a fully-illuminated planetary disk. A fraction of the stellar flux will be scattered by the planetary atmosphere, enabling one to define the *geometric albedo spectrum*:

$$A_g(\lambda) = \left(\frac{a}{R_p} \right)^2 \frac{F_p(\alpha = 0, \lambda)}{F_*(\lambda)} \quad (1)$$

where a is the planet-star orbital separation, R_p is the planetary radius, $F_p(\alpha = 0, \lambda)$ is the observed scattered flux from the fully-illuminated planetary disk (the planet at opposition in solar system parlance), and $F_*(\lambda)$ is the stellar flux. α is the phase angle, defined as the angle between the stellar ray incident of the planet and the ray towards the observer. For transiting exoplanets, the condition of full illumination ($\alpha = 0$) occurs upon star-planet osculation (i.e. secondary eclipse). In practise, observations of reflection spectra will be taken during partial illumination ($\alpha \neq 0$), such that

$$\frac{F_p(\alpha, \lambda)}{F_*(\lambda)} = A_g(\lambda) \left(\frac{R_p}{a} \right)^2 \Phi(\alpha, \lambda) \quad (2)$$

where the decrease in scattered flux is encoded in the phase function, $\Phi(\alpha, \lambda)$ – normalised to 1 when $\alpha = 0$.

When discussing reflection spectra in this work, we express our results in terms of geometric albedo spectra, $A_g(\lambda)$. We note that the expression given in Equation 1 is entirely equivalent to the historical definition of geometric albedo as the ratio of the observed scattered flux from the planet at full illumination to that of an isotropically scattering disk of the same cross sectional area as the planet and placed at the same distance (Seager 2010, Chapter 3). For future work, it would be beneficial to supplant this historical terminology with more intuitive nomenclature better suited to dealing with reflection spectra of exoplanets.

The shape of a geometric albedo spectrum is primarily controlled by the relative contributions of molecular absorption opacity, molecular Rayleigh scattering, and the scattering opacity of condensate clouds. The cloud properties, in turn, are determined by the temperature structure and metallicity of the atmosphere. Radiative transfer of stellar photons impinging on the atmosphere then enables determination of the scattered flux, $F_p(\alpha = 0, \lambda)$, and hence the geometric albedo spectrum. Before elaborating on the details of such a calculation, we first turn to illustrate how these atmospheric properties influence the geometric albedo spectrum of Jupiter.

2.2. Geometric Albedo Spectra of Jupiter

Figure 1 shows the observed disk-averaged albedo spectrum of Jupiter (Karkoschka 1994), along with three models demonstrating the influence of clouds and H₂O vapour. The models assume a 3× solar abundance atmosphere, with the Jovian temperature structure derived from Voyager (Lindal et al. 1981). The spectra of both the models and observations can be broken down into a scattering continuum with embedded absorption features. Especially prominent CH₄ features

are noted at $0.54\mu\text{m}$, $0.62\mu\text{m}$, $0.73\mu\text{m}$, $0.79\mu\text{m}$, $0.89\mu\text{m}$, and $0.99\mu\text{m}$ (Karkoschka 1994; Cahoy et al. 2010). The cloud-free model has a continuum provided by Rayleigh scattering, whilst the models with clouds exhibit a significantly brighter continuum at longer wavelengths due to back-scattering from NH_3 clouds. This brightening substantially additionally enhances the contrast of absorption features at longer wavelengths – an example of clouds enhancing the detection of molecular species in reflection spectra.

Comparing our models to observations, we see that the observed spectrum is generally darker at shorter wavelengths. This is due to our models not including the influence of photochemical hazes present in Jupiter’s upper atmosphere (Marley et al. 1999; Sudarsky et al. 2000). Smaller discrepancies at longer wavelengths are likely due to different cloud properties and deviations between Jupiter’s molecular abundances and the uniform $3\times$ solar abundance ratio we assume. Nevertheless, the general qualitative agreement without parameter tuning to fit the observed spectrum serves as a satisfactory demonstration of the efficacy of our modelling framework.

2.2.1. Jupiter’s Concealed H_2O

To assess the prominence of H_2O vapour absorption in Jupiter’s reflection spectrum, Figure 1 also shows how the model with clouds changes when all H_2O vapour is removed. If H_2O absorption signatures were present in the spectrum, this would result in a higher albedo in regions of high H_2O opacity. Instead, we find this model is everywhere coincident with the model including H_2O , demonstrating that no H_2O absorption features are imprinted in our model Jupiter spectrum. Regarding observational signatures, Karkoschka (1994) noted a slight decrease in Jupiter’s albedo relative to Saturn between $0.92 - 0.95 \mu\text{m}$, coincident with the maximum H_2O opacity in the optical, suggesting that this could potentially be attributed to H_2O absorption. However, this feature was later ascribed to NH_3 (Karkoschka 1998). Thus our models and disk-averaged observations are in concordance that Jupiter displays no prominent H_2O signatures.

To understand why this is the case, Jupiter’s temperature structure (Lindal et al. 1981) is displayed on the right of Figure 1 against condensation curves for NH_3 (Ackerman & Marley 2001, Appendix A) and H_2O (Buck 1981). In a simple conceptual picture, a species existing in vapour form in the deep atmosphere begins to condense once the partial pressure it exerts exceeds the species’ saturation vapour pressure

$$P(T)X_{v,i} \geq P_{\text{vap},i}(T) \quad (3)$$

where $P(T)$ is the atmospheric pressure in a given layer, $X_{v,i}$ is the vapour mixing ratio of species i , and $P_{\text{vap},i}(T)$ is the corresponding vapour pressure of species i . As the saturation vapour pressure sharply decreases with temperature (Figure 1, higher layers satisfy this condition once the partial pres-

sure equals the saturation vapour pressure. Above this point, the species begins to condense and the vapour mixing ratio, decreases such that equality is maintained in Equation 3. This condition is equivalent to finding the deepest layer in which the pressure-temperature (P-T) profile intersects the condensation curve, $P_{\text{vap},i}(T)/X_{v,i}$. Note that the mixing ratio causes condensation curves to shift to higher temperatures as metallicity increases. If no intersection occurs, the species will remain in gaseous form throughout the atmosphere. For Jupiter, Figure 1 demonstrates that intersection occurs for both NH_3 and H_2O , forming clouds at pressures of ~ 0.8 bar and ~ 5 bar respectively, matching well with observations (Atreya et al. 1999). H_2O clouds thus form sufficiently deep that rainout depletes the observable atmosphere of detectable quantities of H_2O vapour. The resulting albedo spectrum is then dominated by the higher-altitude NH_3 clouds and absorption due to CH_4 vapour. Jupiter’s concealed H_2O serves to demonstrate the crucial importance played by the atmospheric temperature structure, which governs both the altitudes where clouds form and the types of cloud present.

2.2.2. Revealing H_2O Absorption Signatures

From examining Jupiter’s temperature structure (Figure 1), one can conceptualise how the broad characteristics of reflection spectra alter for cool giant exoplanets. Consider an exoplanet marginally warmer than Jupiter, such that $T_{\text{eff}} \approx 150$ K. Such a minor perturbation is sufficient to ensure the NH_3 condensation curve is no longer crossed, with the H_2O condensation curve intersection occurring higher in the atmosphere. The anticipated result is an atmosphere whose geometric albedo at longer wavelengths is dominated by reflection from H_2O clouds. Due to the rising H_2O cloud base as a function of temperature, it is expected that the fraction of photons reaching the cloud deck, and hence reflected towards the observer, will increase with temperature. These reflected photons will encounter abundant H_2O vapour on their inbound and outbound trajectories, resulting in observable H_2O absorption signatures. This ‘cloud enhancement’ must exhibit a limiting temperature, as the H_2O clouds themselves will begin to dissipate for even warmer planets. However, this limit must also be metallicity dependant, as the condensation curve for a given pressure shifts to higher temperature for greater deep mixing ratios (Equation 3), allowing H_2O clouds to persist to higher temperatures. Additional factors, such as the gravitational field strength (altering the gradient of the P-T profile in the deep atmosphere) and the sedimentation efficiency (controlling cloud thickness and formation altitude) will also influence the prominence of H_2O signatures. Our objective in this study is to quantify the relative contributions of each of these factors. With a conceptual picture of the principal physical processes established, we now elaborate on the calculation of reflection spectra.

2.3. Modelling Exoplanet Reflection Spectra

Computing a reflection spectrum requires specification of three atmospheric properties: (i) the pressure-temperature profile; (ii) chemical abundances; and (iii) cloud characteristics and optical properties. Given these inputs, the equation of radiative transfer is solved according to the geometry at a specified orbital phase (here, $\alpha = 0$). Figure 2 illustrates the steps involved in our modelling process, each of which we examine in turn.

2.3.1. Temperature Structure

Given a specified metallicity, m , C/O ratio, gravitational field strength, g , internal temperature, T_{int} , and incident flux, F_* , one may iteratively calculate the pressure-temperature structure (P-T profile) of an atmosphere. Such ‘self-consistent’ calculations usually assume radiative-convective equilibrium and chemical equilibrium. In principle, one temperature profile can be computed for each desired point in parameter space (as in Cahoy et al. 2010), though this approach is computationally expensive and can sometimes fail to reach a converged solution, particularly if clouds are included as part of the iteration step (Morley et al. 2014). In this study, where our goal is to compute reflection spectra across a wide swath of parameter space, such an approach is not computationally feasible.

Our approach is to develop an *a priori* determined P-T profile that is able to reproduce the behaviour of self-consistent profiles. We fit a simple two-parameter function of the form

$$T^4(P) = T_0^4 + T_{\text{deep}}^4(P/1000\text{bar}) \quad (4)$$

where T_0 and T_{deep} encode the temperatures of an upper-atmosphere isotherm and the temperature at the 1000 bar level, respectively, to a range of self-consistent P-T profiles computed using the formalism of Fortney et al. (2008). The profiles we consider span m from $1 \times$ to $100 \times$ solar, g from 10 ms^{-2} to 100 ms^{-2} , a from 0.5 AU to 5.0 AU, and all have $T_{\text{int}} = 150 \text{ K}$ and C/O = 0.5. We note that these profiles assume a cloud-free atmosphere. From integrating the thermal emission, we derive the effective temperature, T_{eff} , of each atmosphere. From the totality of these fits, we expand T_0 and T_{deep} as functions of metallicity, gravity, and effective temperature, such that we arrive at analytic expressions for $T_0(\log(m), g, T_{\text{eff}})$ and $T_{\text{deep}}(\log(m), g, T_{\text{eff}})$. The fitting procedure, parameter functional forms, and fitting coefficients are detailed in Appendix A.

The variation of our analytic P-T profile with g , T_{eff} , and $\log(m)$ is shown in Figure 3. The broad trends are as follows: (i) lower gravity planets exhibit sharper adiabats in the deep atmosphere (due to convective onset occurring at lower pressures); (ii) higher effective temperature planets have higher isothermal temperatures and sharper adiabats; (iii) higher metallicity planets are slightly warmer (due to the additional

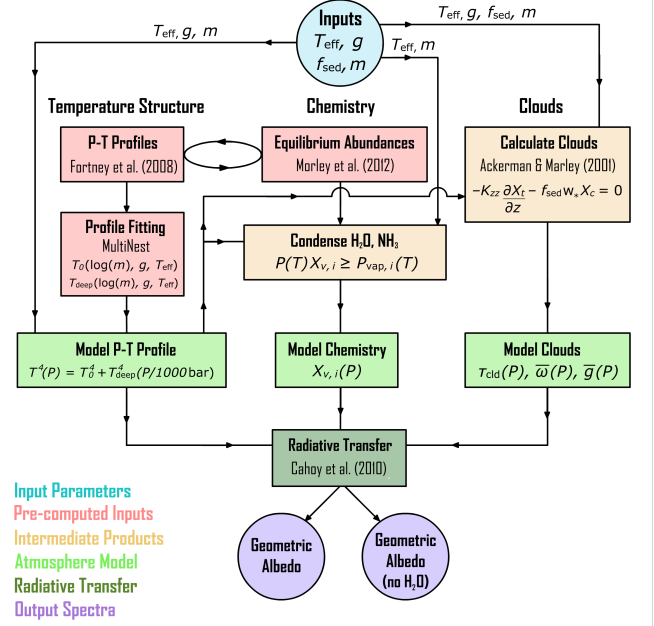


Figure 2. Schematic diagram of our reflection spectra modelling procedure. Arrows indicate operation order, with the loop representing self-consistent iterative coupling. Radiative-convective equilibrium pressure-temperature (P-T) profiles (Fortney et al. 2008) and thermochemical equilibrium abundances (Morley et al. 2012) were pre-computed self-consistently for a grid of cloud-free planets in gravity-distance-metallicity space. A simple parametric function was fit to the equilibrium P-T profiles, yielding $T(P)$ as a function of g , m , and T_{eff} . Where $T(P)$ cross a condensation curve, the equilibrium abundances of condensates are updated due to rainout. For a given $T(P)$, m , f_{sed} , the Ackerman & Marley (2001) cloud model yields the cloud optical depth, single scattering albedo, and asymmetry parameter in each layer. The temperature structure, chemical abundances, and cloud properties are used to solve the equation of radiative transfer Cahoy et al. (2010), yielding two geometric albedo spectra for each value of g , T_{eff} , f_{sed} , and m – one with and one without H₂O vapour opacity.

molecular opacity), but with similar slope adiabats. The simple functional form of our profile allows the computational bottleneck of radiative-convective equilibrium calculations to be circumvented, and hence enables efficient exploration of an extensive region of g - T_{eff} - m parameter space.

2.3.2. Atmospheric Chemistry

At the temperatures relevant to cool giant planets, atmospheres are dominated by H₂ and He, with the principal oxygen, carbon, and nitrogen reservoirs being H₂O, CH₄, and NH₃ (Burrows et al. 1997; Madhusudhan et al. 2016). Our models consider a wide range of chemical species: H₂, He, H⁺, H⁻, H₂O, CH₄, NH₃, CO, CO₂, PH₃, H₂S, N₂, Na, K, TiO, VO, and Fe. The opacities were computed via the k-coefficient method (Freedman et al. 2008), updated for am-

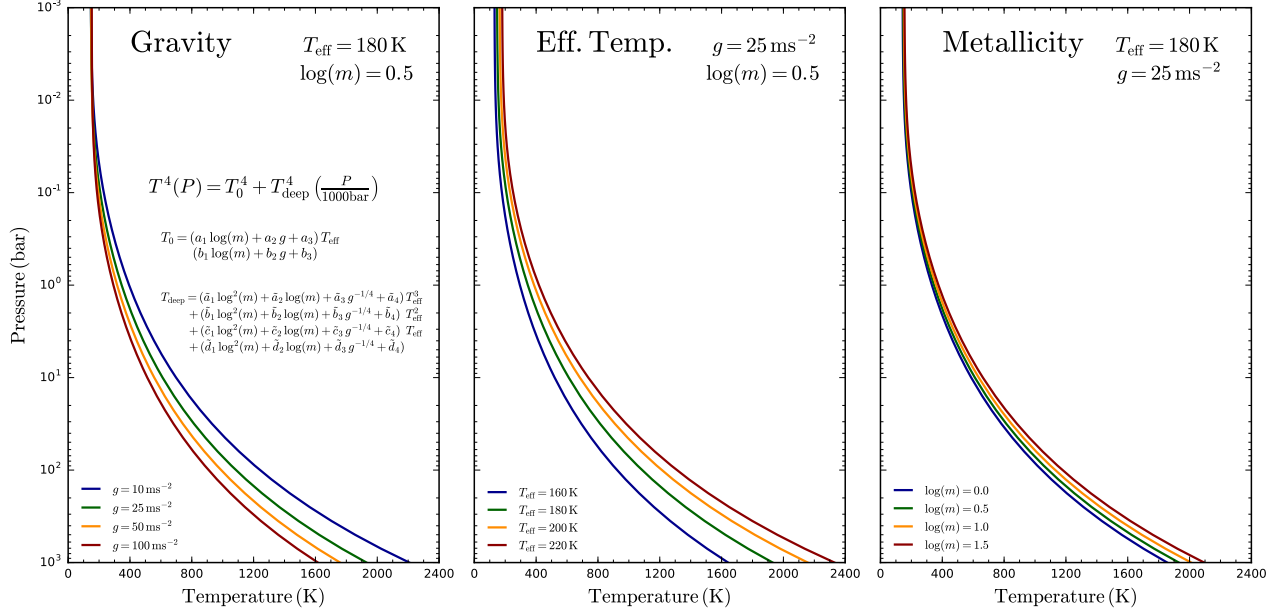


Figure 3. A new analytic P-T profile for cool giant planets. From left to right, the panels show how the temperature structure changes with g , T_{eff} , and m for a reference model with $g = 25 \text{ ms}^{-2}$, $T_{\text{eff}} = 180 \text{ K}$, and $m = 3 \times$ solar. All models assume $T_{\text{int}} = 150 \text{ K}$, and do not explicitly account for clouds. The analytic profile was derived through fitting a grid of radiative-convective equilibrium P-T profiles (Fortney et al. 2008) to a simple parametric function, as detailed in Appendix A.

monia (Yurchenko et al. 2011) and H_2 collisionally-induced opacity (Richard et al. 2012) as described in Saumon et al. (2012). For each of the Fortney et al. (2008) P-T profiles used in the previous section, the abundances of all species were calculated self-consistently assuming thermochemical equilibrium, according to the prescription in Morley et al. (2012). For our purposes, we take the chemistry at each point in parameter space to be representative of the nearest point in the m - T_{eff} plane from the grid of self-consistent models.

As the chemical equilibrium abundances are derived for cloud-free atmospheres, we modify the mixing ratios of NH_3 and H_2O to account for rainout. As a first order correction, we update the vapour mixing ratios following Lewis (1969), starting at the base of the atmosphere and assuming all material in excess of the vapour pressure condenses, such that

$$X_{v,i}(z) = \min[X_{v,i}(z - \Delta z), P_{\text{vap},i}(z)/P(z)] \quad (5)$$

where z specifies the atmospheric layer. The vapour pressures for H_2O and NH_3 are from Buck (1981) and Ackerman & Marley (2001), respectively. This correction is crucial to ensure a degree of consistency between the chemical abundances employed in the geometric albedo calculation and the generated cloud profile (section 2.3.3). Despite this correction, we note that the usage of a stand-alone cloud model is not strictly self-consistent with the chemical abundances, despite using the same P-T profile for both calculations. However, our cloud model features a more sophisticated treatment of condensation than Equation 5, as we shall now see.

2.3.3. Cloud Model

We model H_2O and NH_3 clouds via the prescription of Ackerman & Marley (2001). This model balances the upwards flux of condensate and vapour due to turbulent mixing with the downwards flux of condensate due to sedimentation. For each condensing species, this implies

$$-K_{zz} \frac{\partial X_t}{\partial z} - f_{\text{sed}} w_* X_c = 0 \quad (6)$$

where K_{zz} is the vertical eddy diffusion coefficient, $X_t = X_v + X_c$ is the total combined species mixing ratio of vapour and condensate, w_* is the convective velocity scale, and f_{sed} is a tunable parameter called the *sedimentation efficiency*. Physically, greater values of f_{sed} lead to larger condensate particle sizes with more efficient rainout, and hence thinner cloud profiles. K_{zz} and w_* are both determined via mixing length theory, assuming the diffusion coefficient corresponding to free convective heat transport (Gierasch & Conrath 1985) is equal to K_{zz} . In convectively stable regions, a minimum value of $K_{zz} = 10^5 \text{ cm}^2 \text{ s}^{-1}$ is prescribed to account for sources of residual turbulence in radiative regions. With f_{sed} and the atmospheric metallicity, m (controlling the deep mixing ratios of H_2O and NH_3), specified, Equation 6 is solved for the condensate mixing ratio in each layer, assuming that all excess vapour condenses (Equation 3).

Once the condensate mixing ratios are determined, the next step is the specification of a condensate particle size distribu-

tion. For this purpose, we assume each condensed species follows a lognormal distribution:

$$\frac{dn}{dr} = \frac{N}{r\sqrt{2\pi}\ln\sigma_g} e^{-\frac{\ln^2(r/r_g)}{2\ln^2\sigma_g}} \quad (7)$$

where $n(r)$ is the number density of condensate particles with radii $< r$, N is the total number density for a given condensate, r_g is the geometric mean radius, and σ_g is the geometric standard deviation (here set to be 2.0 throughout). Full specification of this distribution requires determination of r_g , accomplished by interpreting $f_{\text{sed}} w_*$ as the mass-weighted sedimentation velocity:

$$f_{\text{sed}} w_* = \frac{\int_0^\infty v_f(r) r^3 \frac{dn}{dr} dr}{\int_0^\infty r^3 \frac{dn}{dr} dr} \quad (8)$$

where $v_f(r)$ is the particle ‘fall’ speed at a given radius - calculated assuming viscous flow around spherical particles and corrected for kinetic effects (see Ackerman & Marley 2001, Appendix B). Substituting Equation 7 into Equation 8 and evaluating the integrals then yields r_g . N can similarly be obtained by integrating Equation 7 which, together with r_g , fully specifies the distribution in terms of the only remaining free parameter, f_{sed} .

With the size distribution determined, the cloud scattering properties are calculated using Mie theory. We assume spherical, homogeneous, particles. The complex refractive indices of H₂O ice (Warren 1984) and NH₃ ice (Martonchik et al. 1984) are utilised to evaluate the Mie efficiencies at 2000 uniformly-spaced wavelengths from 0.3 - 1.0 μm . The efficiencies are then integrated over the particle size distribution in Equation 7 to produce the single scattering albedo, $\tilde{\omega}$, asymmetry parameter, \tilde{g} , and cloud optical depth, τ_{cld} , in each atmospheric layer as a function of wavelength.

2.3.4. Radiative Transfer

Having specified the temperature structure, chemical abundances, and cloud properties as a function of altitude, the equation of radiative transfer is solved to compute the scattered flux from the planetary atmosphere. We evaluate the geometric albedo using the approach developed by Toon et al. (1977, 1989); McKay et al. (1989a); Marley et al. (1999); Marley & McKay (1999) and extended to arbitrary phase angles by Cahoy et al. (2010). In this approach, the planetary hemisphere is divided into a number of plane-parallel facets. Each of these facets represents an atmospheric column in which 1D radiative transfer, including multiple scattering, is evaluated. We calculate radiative transfer as described in McKay et al. (1989a) and Marley et al. (1999). Other applications and further details can be found in McKay et al. (1989a,b); Marley et al. (1996); Burrows et al. (1997);

Marley & McKay (1999); Marley et al. (2002); Saumon & Marley (2008); Fortney et al. (2008); Cahoy et al. (2010). We assume the same P-T profile, chemistry, and cloud properties are present in each column – effectively representing hemispheric average properties. However, since each facet experiences different angles for both the incident stellar flux and the angle to the observer, the scattered flux will vary with latitude and longitude. The observed geometric albedo is then produced via Chebyshev-Gauss integration over the hemisphere’s two dimensional coordinate system to average over viewing geometry (see Cahoy et al. 2010, for greater detail). We typically evaluate geometric albedo spectra at 2000 wavelengths, uniformly-spaced from 0.3 to 1.0 μm .

This framework gives the flexibility to explore an extensive parameter space. Our P-T profiles are directly specified as functions of g , T_{eff} , and $\log(m)$; chemistry as a function of m and T_{eff} ; and cloud properties as a function of m and f_{sed} . The chemistry and cloud properties are also indirectly influenced by the other parameters through the shape of the P-T profile (see Figure 2). We can thus model reflection spectra of exoplanetary atmospheres spanning the 4-dimensions of T_{eff} , g , m , and f_{sed} . For each point in parameter space, we generate two geometric albedo spectra: one following the prescription as described above, and a second where we artificially remove all H₂O vapour opacity during the radiative transfer calculation. It is the differences between these two models that enables us to assess the prominence of H₂O absorption in the atmosphere.

3. FACTORS INFLUENCING H₂O PROMINENCE IN COOL GIANT PLANETS

We begin our investigation into H₂O signatures in cool giant planets by examining the spectral regions in which they occur and how their prominence is affected by planetary parameters. We consider, in turn, the impact of effective temperature, gravity, sedimentation efficiency, and metallicity. Specifically, we take a reference giant planet model with $T_{\text{eff}} = 180$ K, $g = 10$ ms^{-2} , $f_{\text{sed}} = 3$, and $m = 3 \times$ solar, examining how H₂O signatures change as each parameter is perturbed. We choose this reference model to be ~ 60 K warmer than Jupiter, such that NH₃ clouds do not form and hence weak H₂O signatures are already visible for such a planet.

3.1. Effective Temperature

Figure 4 demonstrates how changes in T_{eff} affect geometric albedo spectra of cool giant planets. In general, cooler planets are brighter, especially at longer wavelengths, whilst warmer planets are darker at most wavelengths. H₂O absorption features are seen even for the coolest model shown ($T_{\text{eff}} = 160$ K). Prominent H₂O absorption is seen from $\sim 0.91 - 0.98$ μm and $\sim 0.79 - 0.86$ μm , coinciding with the first and second maxima of the H₂O optical opacity, and across a forest of

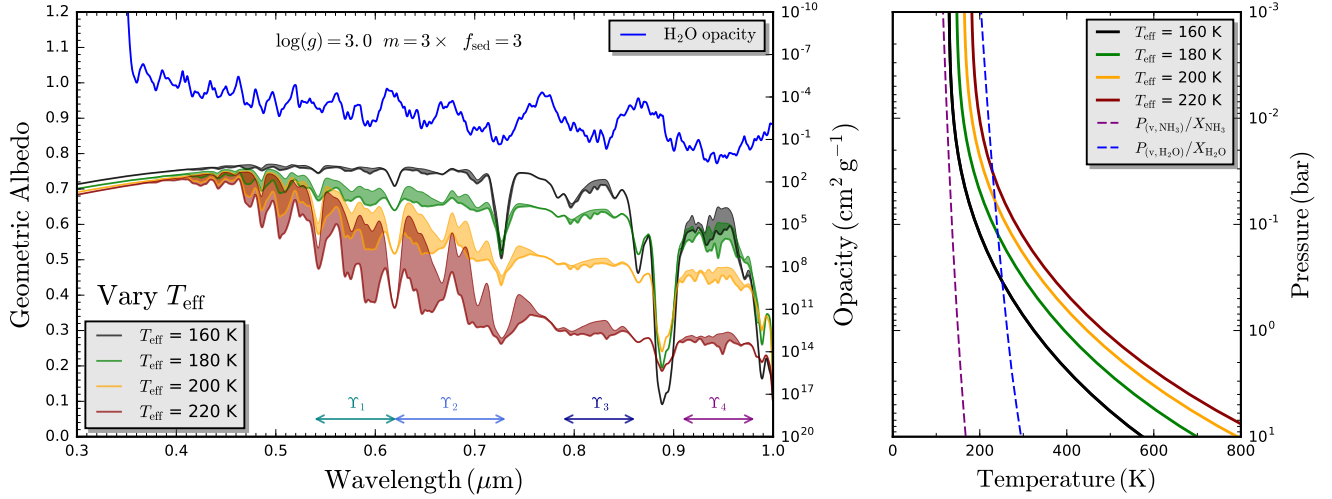


Figure 4. The influence of effective temperature on H₂O absorption signatures in reflection spectra of cool giant planets. Left: geometric albedo spectra models of four planets, with $T_{\text{eff}} = 160$ K (black), 180 K (green), 200 K (orange), and 220 K (red). All planets have $g = 10 \text{ ms}^{-2}$ ($\log(g)$ (cgs) = 3.0, $m = 3 \times$ solar, and $f_{\text{sed}} = 3$). The green model is a common reference in Figures 4, 5, 7, and 6. Two models are plotted for each planet: one with H₂O opacity enabled (lower curve), and one without H₂O opacity (upper curve), with the region between the models shaded. The shaded region thus indicates H₂O absorption signatures. The H₂O opacity is shown in blue (smoothed for clarity). Four spectral regions with prominent H₂O signatures are indicated by $\Upsilon_{1,2,3,4}$ (see Section 4.1). Right: P-T profiles corresponding to the same four planet models, with the NH₃ (purple) and H₂O (blue) condensation curves for a $3 \times$ solar atmosphere.

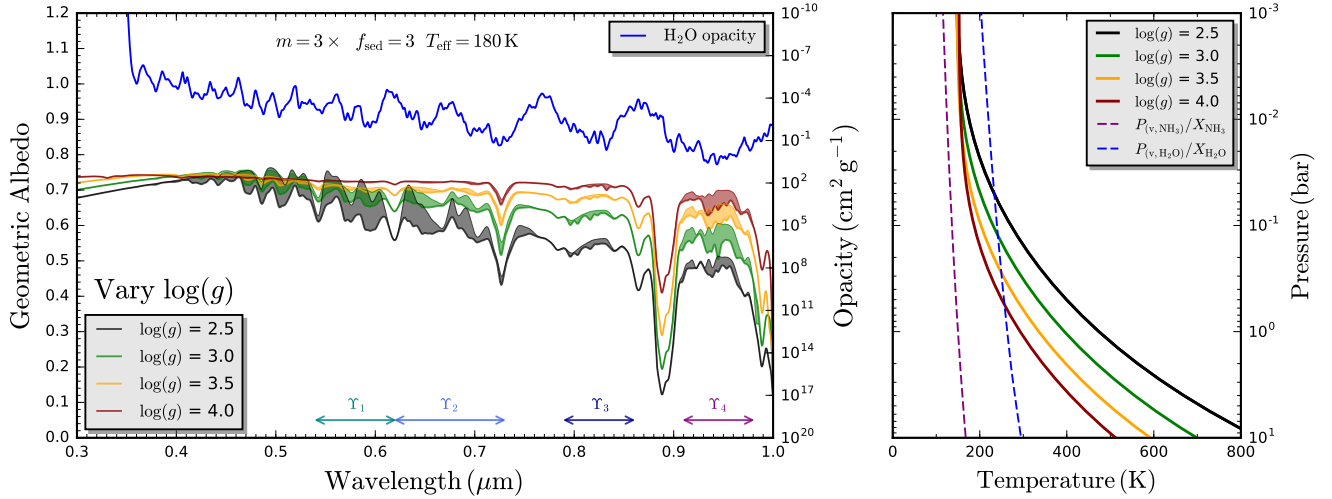


Figure 5. The influence of gravity on H₂O absorption signatures in reflection spectra of cool giant planets. Left: geometric albedo spectra models of four planets, with $\log(g)$ (cgs) = 2.5 (black), 3.0 (green), 3.5 (orange), and 4.0 (red) – corresponding to $g = 3.16, 10.0, 31.6,$ and 100.0 ms^{-2} , respectively. All planets have $m = 3 \times$ solar, $f_{\text{sed}} = 3$, and $T_{\text{eff}} = 180$ K. The green model is a common reference in Figures 4, 5, 7, and 6. Two models are plotted for each planet: one with H₂O opacity enabled (lower curve), and one without H₂O opacity (upper curve), with the region between the models shaded. The shaded region thus indicates H₂O absorption signatures. The H₂O opacity is shown in blue (smoothed for clarity). Four spectral regions with prominent H₂O signatures are indicated by $\Upsilon_{1,2,3,4}$ (see Section 4.1). Right: P-T profiles corresponding to the same four planet models, with the NH₃ (purple) and H₂O (blue) condensation curves for a $3 \times$ solar atmosphere.

features from $\sim 0.4 - 0.73 \mu\text{m}$. These regions are indicated in Figure 4 by $\Upsilon_{1,2,3,4}$, where we have split the ‘H₂O forest’ into two regions, taking the CH₄ features at 0.54, 0.62, and $0.73 \mu\text{m}$ as natural dividers. The prominence of H₂O absorp-

tion in these regions will be quantitatively explored in terms of spectral indices in Section 4. H₂O absorption features at $< 0.54 \mu\text{m}$ may suffer from darkening due to photochemical hazes (see Figure 1), leading to an overstatement of their

prominence in our model spectra, so for this reason we do not assign these features a separate spectral index.

The strength of H₂O absorption features can vary dramatically with temperature. For $\lambda \lesssim 0.8 \mu\text{m}$ H₂O signatures are strongest for high T_{eff} , whilst the $0.94 \mu\text{m}$ feature is strongest for lower T_{eff} . The feature around $0.83 \mu\text{m}$ represents an intermediate case that is relatively insensitive to T_{eff} . These trends are caused by τ_{cld} decreasing for planets with greater T_{eff} , due to the P-T profile intersecting the H₂O condensation curve at higher altitudes where the lower pressure results in less mass of H₂O being available to condense (Equation 3). Specifically, the peak values of the cloud optical depth, $\tau_{\text{cld,max}}$, are 74, 22, 8, and 3 for $T_{\text{eff}} = 160 \text{ K}$, 180 K , 200 K , and 220 K , respectively. For low temperature planets the albedo is thus dominated by the highly reflective ($\bar{\omega} > 0.999$) H₂O clouds, which provide a backscattering surface for photons at long wavelengths. The H₂O feature around $0.94 \mu\text{m}$ is the most prominent for such cool planets due to its greater opacity. At higher temperatures, the optically thin clouds are less effective at reflecting photons and hence more are lost to the deep atmosphere, resulting in both a darker planet and a weaker $0.94 \mu\text{m}$ feature. However, the H₂O features for $\lambda \lesssim 0.8 \mu\text{m}$ increase in prominence at higher T_{eff} due to Rayleigh scattering providing a cloud-independent avenue for short wavelength photons to probe the deep atmosphere, accrue absorption features, and emerge unscathed.

We note in passing that many of these trends can be understood qualitatively by examining the toy cloud model discussed in Marley (2000). Cloud opacity depends on the available column mass of material that can condense, which itself depends on gravity, temperature, and cloud base pressure.

3.2. Gravity

Figure 5 demonstrates how changes in g affect geometric albedo spectra. Gravitational field strength contributes to the spectra in two principal ways: (i) changing the P-T profile, thereby affecting cloud formation; (ii) changing the density scale height of the atmosphere. (i) is by far the dominant of these effects, as changes in the cloud optical depth and pressure level controls both the overall reflectivity of the atmosphere and the prominence of H₂O features. As higher gravity planets have steeper P-T profiles, they intersect the H₂O vapour pressure curve lower in the atmosphere, hence forming deep, optically thick, cloud decks ($\tau_{\text{cld,max}} \approx 50$ for the $\log(g) = 4.0$ (cgs) in Figure 5). This results in bright albedo spectra with the $0.94 \mu\text{m}$ H₂O feature most prominent. Planets with low g exhibit ‘gravity enhanced’ H₂O features below $0.8 \mu\text{m}$ due to Rayleigh scattering dominating when τ_{cld} is low – similar to the trend seen for high T_{eff} planets in section 3.1. (ii) generally results in stronger H₂O features for lower g , as the larger density scale height raises the column abundance of H₂O encountered by photons before backscattering

at a given pressure level. The compound effect of (i) and (ii) is thus a substantial gravity enhancement in H₂O features $< 0.8 \mu\text{m}$ for planets with $g \lesssim 10 \text{ ms}^{-2}$.

3.3. Sedimentation Efficiency

Figure 6 demonstrates how changes in f_{sed} affect geometric albedo spectra. Generally, higher sedimentation efficiencies lead to darker planets with deeper H₂O absorption features. Unlike for T_{eff} and g , this is not caused by changes in the location of the cloud base. Clouds begin to form at a common value of $\sim 250 \text{ mbar}$ for the depicted models, as our P-T profile parametrisation is invariant to f_{sed} (section 2.3.1). Rather, the relevant factor here is the cloud thickness above the base, which controls the overall optical depth of the cloud layer. Greater values of f_{sed} result in larger mean particle radii, leading to more efficient rainout and hence thinner clouds (section 2.3.3). Specifically, for the four models shown in Figure 6, the cloud vertical extents with $\tau_{\text{cld}} > 1$ in each layer are $\sim 20\text{-}250 \text{ mbar}$, $50\text{-}250 \text{ mbar}$, $60\text{-}250 \text{ mbar}$, and $90\text{-}250 \text{ mbar}$; for $f_{\text{sed}} = 1, 3, 5,$ and 7 , respectively. $\tau_{\text{cld,max}}$ in each case is 84, 22, 12, and 7, occurring around 130 mbar . We see then that the thickest clouds in vertical extent are also the most efficient at scattering, explaining the high albedo for models with low f_{sed} . Models with higher f_{sed} then display stronger H₂O features due to the greater path length traversed before encountering the upper edge of the cloud deck. H₂O absorption at $0.94 \mu\text{m}$ thus becomes more prominent for higher f_{sed} , but at the cost of a lower continuum albedo due to less photons reaching the clouds when the upper edge is at deeper pressures. However, features below $0.8 \mu\text{m}$ have the benefit of an underlying Rayleigh scattering continuum, leading to H₂O features which stand out against a bright continuum for high f_{sed} .

3.4. Metallicity

Figure 7 demonstrates how changes in m affect geometric albedo spectra. Three trends emerge as metallicity increases: (i) CH₄ absorption features strengthen; (ii) the continuum albedo brightens; (iii) H₂O absorption features weaken. The strengthening of CH₄ features can be seen most strikingly around $0.73 \mu\text{m}$ and $0.89 \mu\text{m}$, which is simply a consequence of the increased CH₄ abundance for models with higher m . At first glance, it is somewhat counter-intuitive that H₂O features do not strengthen in the same manner, despite the increased H₂O abundance. This difference can be understood in terms of H₂O condensation, as CH₄ exists in vapour form throughout the atmosphere (condensing only for $T_{\text{eff}} \lesssim 100 \text{ K}$). First, note that the H₂O condensation curves and P-T profiles intersect at roughly the same pressure (Figure 7, right), so the cloud bases occur at similar altitudes. However, higher m implies higher deep abundances, increasing the H₂O partial pressure, and thereby causing an expanded inventory of

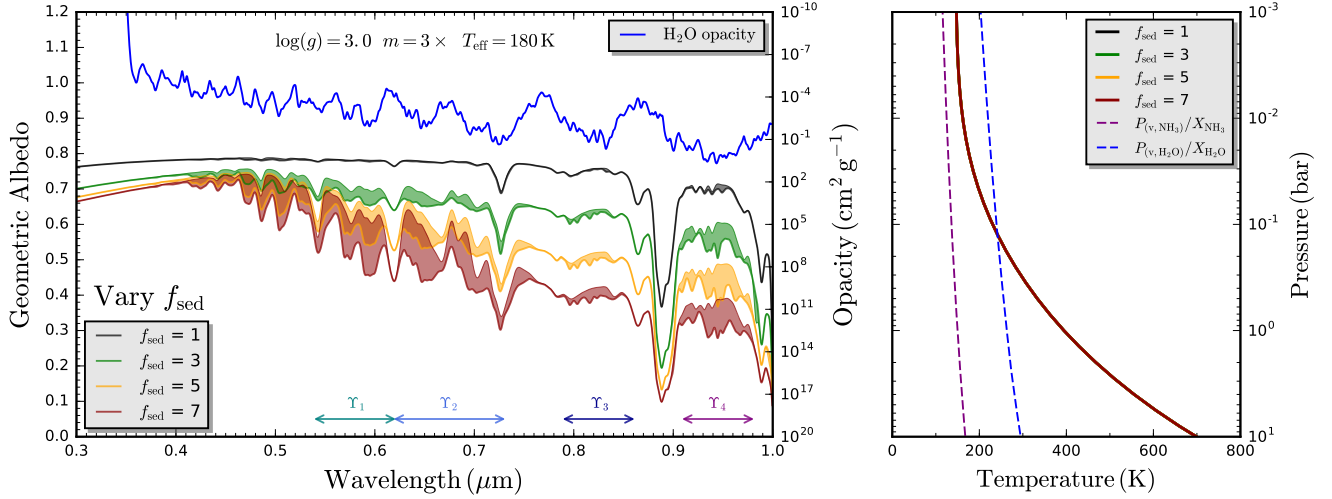


Figure 6. The influence of sedimentation efficiency on H₂O absorption signatures in reflection spectra of cool giant planets. Left: geometric albedo spectra models of four planets, with $f_{\text{sed}} = 1$ (black), 3 (green), 5 (orange), and 7 (red). All planets have $g = 10 \text{ ms}^{-2}$ ($\log(g)$ (cgs) = 3.0), $m = 3 \times$ solar, and $T_{\text{eff}} = 180 \text{ K}$. The green model is a common reference in Figures 4, 5, 7, and 6. Two models are plotted for each planet: one with H₂O opacity enabled (lower curve), and one without H₂O opacity (upper curve), with the region between the models shaded. The shaded region thus indicates H₂O absorption signatures. The H₂O opacity is shown in blue (smoothed for clarity). Four spectral regions with prominent H₂O signatures are indicated by $\Upsilon_{1,2,3,4}$ (see Section 4.1). Right: P-T profiles corresponding to the same four planet models, with the NH₃ (purple) and H₂O (blue) condensation curves for a $3 \times$ solar atmosphere. Note that the four P-T profiles are coincident, as our temperature profile is invariant to cloud properties (Section 2.3.1).

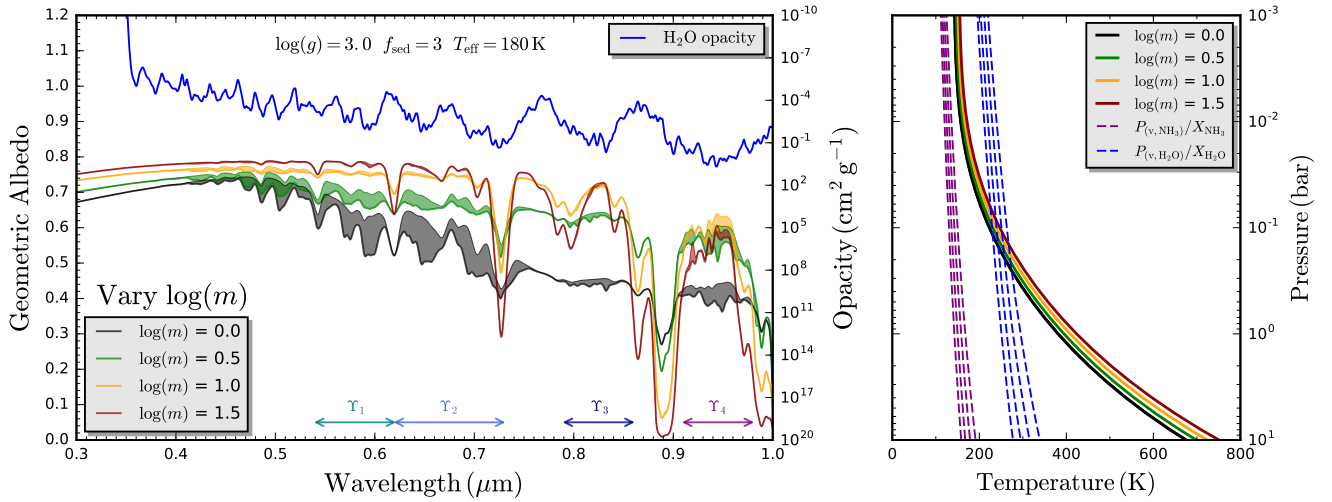


Figure 7. The influence of metallicity on H₂O absorption signatures in reflection spectra of cool giant planets. Left: geometric albedo spectra models of four planets, with $\log(m) = 0.0$ (black), 0.5 (green), 1.0 (orange), and 1.5 (red) \times solar – corresponding to $m = 1.00, 3.16, 10.0,$ and $31.6 \times$ solar, respectively. All planets have $g = 10 \text{ ms}^{-2}$ ($\log(g)$ (cgs) = 3.0), $f_{\text{sed}} = 3$, and $T_{\text{eff}} = 180 \text{ K}$. The green model is a common reference in Figures 4, 5, 7, and 6. Two models are plotted for each planet: one with H₂O opacity enabled (lower curve), and one without H₂O opacity (upper curve), with the region between the models shaded. The shaded region thus indicates H₂O absorption signatures. The H₂O opacity is shown in blue (smoothed for clarity). Four spectral regions with prominent H₂O signatures are indicated by $\Upsilon_{1,2,3,4}$ (see Section 4.1). Right: P-T profiles corresponding to the same four planet models, with the NH₃ (purple) and H₂O (blue) condensation curves for each metallicity value, with metallicity increasing from left to right.

condensed H₂O. The result is the formation of increasingly optically thick clouds ($\tau_{\text{cl,max}} = 6, 22, 79, 204$, for $\log(m)$

$= 0.0, 0.5, 1.0,$ and 1.5), which form a bright backscattering surface that dominates over all other opacity for high m .

4. MAXIMISING DETECTABILITY OF H₂O IN COOL GIANT PLANETS

Having demonstrated how reflection spectra and H₂O features qualitatively change with planetary properties, in this section we proceed to identify regions of parameter space with maximally prominent H₂O signatures. We begin by introducing a quantitative measure of the observability of H₂O signatures, before utilising this metric to extend the results of the previous section to thousands of model atmospheres.

4.1. Quantifying H₂O Observability

Signatures of H₂O manifest via irregular perturbations to the continuum, prohibiting standard absorption feature metrics such as equivalent width (Chamberlain & Hunten 1987). Therefore, we develop a quantitative prescription for evaluating the observability of H₂O based on two factors: (i) the strength of H₂O absorption features; (ii) the continuum albedo inside the absorbing window. A balance must be established between these factors, as even a strong H₂O feature will not be observable if it results in a planet sufficiently dark to render albedo measurements infeasible. With this compromise in mind, we propose spectral indices of the form:

$$\Upsilon_i = 4 \frac{\overline{\Delta A_g}}{\overline{A_g}} \quad (9)$$

where $\overline{\Delta A_g} = (\overline{A_{g, \text{noH}_2\text{O}}} - \overline{A_g})$ is the mean difference between the geometric albedos of two models without and with H₂O vapour opacity enabled, and $\overline{A_g}$ is the mean continuum geometric albedo (with H₂O opacity). The factor of 4 is an arbitrary constant set such that $\Upsilon_{i, \text{max}} = (\overline{A_{g, \text{noH}_2\text{O}}})^2$, occurring when $\overline{A_g} = (1/2)\overline{A_{g, \text{noH}_2\text{O}}}$. The index i indicates the spectral range over which mean quantities are evaluated, e.g:

$$\overline{\Delta A_g} = \frac{1}{\lambda_2 - \lambda_1} \int_{\lambda_1}^{\lambda_2} [A_{g, \text{noH}_2\text{O}}(\lambda) - A_g(\lambda)] d\lambda \quad (10)$$

where the pairs of values (λ_1, λ_2) for each spectral index are as follows: $\Upsilon_1 \in (0.54 \mu\text{m}, 0.62 \mu\text{m})$; $\Upsilon_2 \in (0.62 \mu\text{m}, 0.73 \mu\text{m})$; $\Upsilon_3 \in (0.79 \mu\text{m}, 0.86 \mu\text{m})$; $\Upsilon_4 \in (0.91 \mu\text{m}, 0.98 \mu\text{m})$.

We demonstrate the calculation of the spectral indices Υ_i for a model reflection spectrum in Figure 8. This figure also provides a convenient geometrical picture of the terms in Equation 9. $\overline{\Delta A_g}$ is simply the coloured area within a given spectral region divided by the width of the region. $\overline{A_g}$, shown by the black arrows, provides a measure of the continuum albedo which would be observed within a given spectral region. As the enclosed area increases (due to greater H₂O absorption), the black arrows necessarily decrease, resulting in their product exhibiting a maximum value when $\overline{\Delta A_g} = \overline{A_g} = (1/2)\overline{A_{g, \text{noH}_2\text{O}}}$ (i.e. the shaded region has a width-averaged height equal to the black arrow). We thus see that Υ_i favours planets with deep H₂O features that also

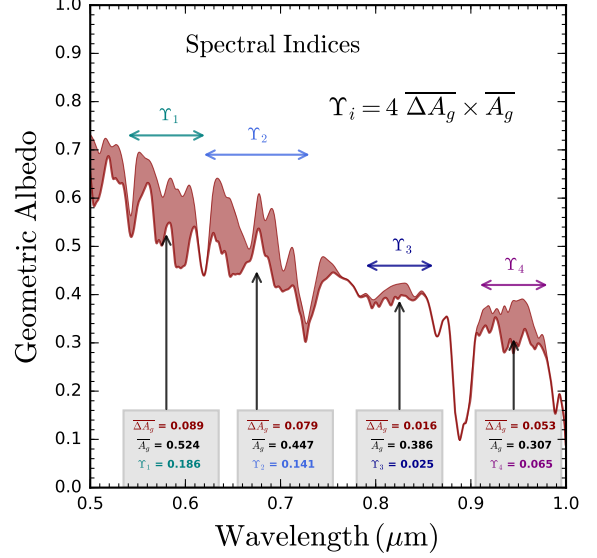


Figure 8. A quantitative prescription for evaluating H₂O prominence in reflection spectra. The bold red curve shows the geometric albedo spectrum of a model with $g = 10 \text{ ms}^{-2}$, $m = 3 \times \text{solar}$, $f_{\text{sed}} = 7$, and $T_{\text{eff}} = 180 \text{ K}$. The light red curve shows the geometric albedo of an identical model with H₂O vapour opacity disabled, such that the enclosed red shaded region is caused by H₂O absorption. Four spectral regions with prominent H₂O features are indicated. The black arrows show the mean geometric albedo, $\overline{A_g}$, within each spectral region. Spectral indices Υ_i are calculated for each region using Equations 9 and 10, resulting in the values in the boxes.

posses a reasonable continuum albedo, enshrining the desired compromise wherein observable H₂O features arise.

4.2. Exploring H₂O Prominence

We now proceed to explore the prominence of H₂O features across a wide range of atmospheric models. We saw in Section 3 that H₂O signatures are influenced by changes in T_{eff} , g , f_{sed} , and m , and, crucially, that a parameter change that enhances H₂O features at short wavelengths can simultaneously weaken them at long wavelengths. With spectral indices on hand, we shall generalise these conclusions by systematically computing the prominence of H₂O features in multiple spectral regions for an ensemble of models.

We consider the 4-dimensional parameter space spanned by T_{eff} , g , f_{sed} , and m . Our models range from $T_{\text{eff}} = 150 \rightarrow 400 \text{ K}$, $\log(g) = 2.0 \rightarrow 4.0$ (cgs), $f_{\text{sed}} = 1 \rightarrow 10$, and $\log(m) = 0.0 \rightarrow 2.0 \times \text{solar}$. We discretise this parameter space into intervals of $\Delta T_{\text{eff}} = 10 \text{ K}$, $\Delta \log(g) = 0.1 \text{ dex}$, $\Delta f_{\text{sed}} = 1$, and $\Delta \log(m) = 0.5 \text{ dex}$, generating reflection spectra both with and without H₂O opacity enabled via the methodology outlined in Section 2.3. The resulting 54,600 geometric albedo spectra are provided for the community¹.

¹ Reflection Spectra Repository

The reasoning behind the chosen parameter space is as follows. Our coolest models are ~ 30 K warmer than Jupiter, set by the requirement that $T_{\text{eff}} > T_{\text{int}}$ (our P-T profiles are based on models with $T_{\text{int}} = 150$ K – see Appendix A). The warmest models ($T_{\text{eff}} \sim 400$ K) correspond to $a \sim 0.5$ AU around a solar analogue, sufficient to cover exoplanets explorable by the inner working angles anticipated of upcoming direct imaging missions. The range of g from $1 \text{ ms}^{-2} \rightarrow 100 \text{ ms}^{-2}$ was chosen to include a wide range of possible surface gravities for radial-velocity planets with known values of $M \sin(i)$. Similarly, m was chosen to range from $1 \rightarrow 100\times$ solar to encompass a wide range of possible atmospheric metallicities. Typical values of f_{sed} considered to date have varied from 1–3 for planets (Ackerman & Marley 2001), up to 6 for brown dwarfs (Stephens et al. 2009), and as high as 10 for some cool giant planets (Cahoy et al. 2010). Values as small as $f_{\text{sed}} = 0.01$ have also been considered to explain flat transmission spectra (Kreidberg et al. 2014a; Morley et al. 2015). We chose $f_{\text{sed}} = 1$ as a minimum boundary, as smaller values produce thick highly-extended clouds that lead to uniformly bright albedo spectra with few absorption features (Morley et al. 2015). The maximum value of $f_{\text{sed}} = 10$ was chosen to encompass physically motivated plausible values.

The prominence of H₂O signatures across this 4-dimensional parameter space is shown in Figure 9. We demonstrate how the observability of H₂O varies across a series of $f_{\text{sed}} - T_{\text{eff}}$ planes, quantified by the spectral indices Υ_1 (left) and Υ_4 (right). Υ_1 represents H₂O signatures along the Rayleigh scattering slope ($\sim 0.6 \mu\text{m}$), whilst Υ_4 represents H₂O signatures around the optical opacity maximum ($\sim 0.94 \mu\text{m}$). We do not show Υ_2 or Υ_3 , as the former displays the same trends as Υ_1 , whilst the latter tends to be less prominent than the other spectral indices (e.g., Figure 8). Each $f_{\text{sed}} - T_{\text{eff}}$ plane contains 160 values of Υ_1 or Υ_4 , interpolated using a rectangular bivariate spline of cubic order to produce contour maps. The blue regions contain negligible H₂O absorption, whilst the red correspond to highly prominent H₂O features. The variation with g and m are shown in the animated version of Figure 9 (available online in the HTML representation of this study), whilst the static version is for a representative planet with $g = 10 \text{ ms}^{-2}$ and $m = 3\times$ solar.

Two distinct avenues exist to maximise H₂O prominence: (i) planets with deep, highly reflective, clouds observed at long wavelengths; (ii) planets with weak, optically thin, clouds at short wavelengths. The difference primarily stems from the wavelength dependence of Rayleigh scattering. Long wavelength H₂O features have strong H₂O opacity but little Rayleigh scattering, thus requiring clouds to provide a continuum. Short wavelength features can rely on a Rayleigh continuum, but their lower H₂O opacity necessitates longer path lengths to accrue H₂O signatures; thus favouring optically thin clouds. These two regions can be seen in Figure

9, with an ‘island’ of prominent long wavelength H₂O absorption from avenue (i) on the right, and a vast plateau of prominent short wavelength H₂O absorption from avenue (ii) on the left. The distinction between these two regions is primarily due to T_{eff} . Low T_{eff} (~ 150 K) results in the deep optically thick clouds favoured by Υ_4 , whilst $T_{\text{eff}} \gtrsim 180$ K results in weaker clouds favoured by Υ_1 . A maximum in Υ_1 occurs just prior to the dissipation of H₂O clouds ($T_{\text{eff}} \sim 230$ K), caused by cloud backscattering enhancing the continuum albedo above that of Rayleigh scattering (favoured by the second term in Equation 9). This ‘cloud enhanced’ region is a general feature of Υ_1 and Υ_2 . Higher values of f_{sed} , resulting in thinner and deeper clouds, tends to enhance both Υ_1 and Υ_4 due to the increased path length traversed before scattering occurs. As the observability of Υ_4 is critically dependant on clouds, values of $f_{\text{sed}} \gtrsim 3$ are typically required to ensure prominent long wavelength features. For larger values of f_{sed} than considered here (>10), Υ_4 rapidly falls as efficient particle sedimentation produces optically-thin clouds, leaving planets dark at long wavelengths (e.g. Figure 6).

Metallicity influences the prominence of both short and long wavelength H₂O signatures across the entire $f_{\text{sed}} - T_{\text{eff}}$ plane. Generally speaking, Υ_1 and Υ_4 rise from solar metallicity until $\log(m) \sim 0.5\times$ solar, then steadily fall as m rises further. The initial rise in prominence is caused by the increased atmospheric H₂O vapour abundance (and brighter continuum due to enhanced H₂O cloud scattering), with the decrease caused by high cloud optical depths dominating spectra (e.g. Figure 7). The regions of maximal H₂O prominence shift to higher T_{eff} as m increases, due to shifting H₂O condensation curves. The Υ_1 ‘cloud-enhanced’ region shifts and contracts from $T_{\text{eff}} \sim 210 - 240 \text{ K} \rightarrow \sim 240 - 250 \text{ K}$ for $m = 1 \rightarrow 100\times$ solar and $f_{\text{sed}} \sim 3$, whilst the Υ_4 ‘H₂O island’ shifts and expands from $T_{\text{eff}} \sim 150 - 160 \text{ K} \rightarrow \sim 200 - 250 \text{ K}$ (Figure 9, animation).

Gravitational field strength plays a crucial role in determining the relative prominences of short wavelength and long wavelength H₂O signatures. Υ_1 is essentially 0 for $g \sim 100 \text{ ms}^{-2}$, but rapidly rises as g lowers. Υ_4 instead tends to rise for higher g , with the maximal values of Υ_1 and Υ_4 in the $f_{\text{sed}} - T_{\text{eff}}$ plane reaching parity at $g \approx 20 \text{ ms}^{-2}$. This differing behaviour is due to low gravity planets forming optically thin cloud decks, as seen in Section 3.2 (the CH₄ clouds of Uranus being a typical example). This dichotomy presents an intriguing possibility: planets with $g \lesssim 20 \text{ ms}^{-2}$ should display H₂O features that are substantially more detectable at wavelengths $< 0.8 \mu\text{m}$ than around the $0.94 \mu\text{m}$ H₂O feature. This conclusion holds true over a vast parameter space, relatively independent of f_{sed} and m , and for $T_{\text{eff}} \gtrsim 180 \text{ K}$ when $f_{\text{sed}} \lesssim 6$ (Figure 9, animation). On the other hand, planets with $g \gtrsim 20 \text{ ms}^{-2}$ may offer better prospects of detecting H₂O around $0.94 \mu\text{m}$ – if the values of T_{eff} , f_{sed} , and m are right to enable

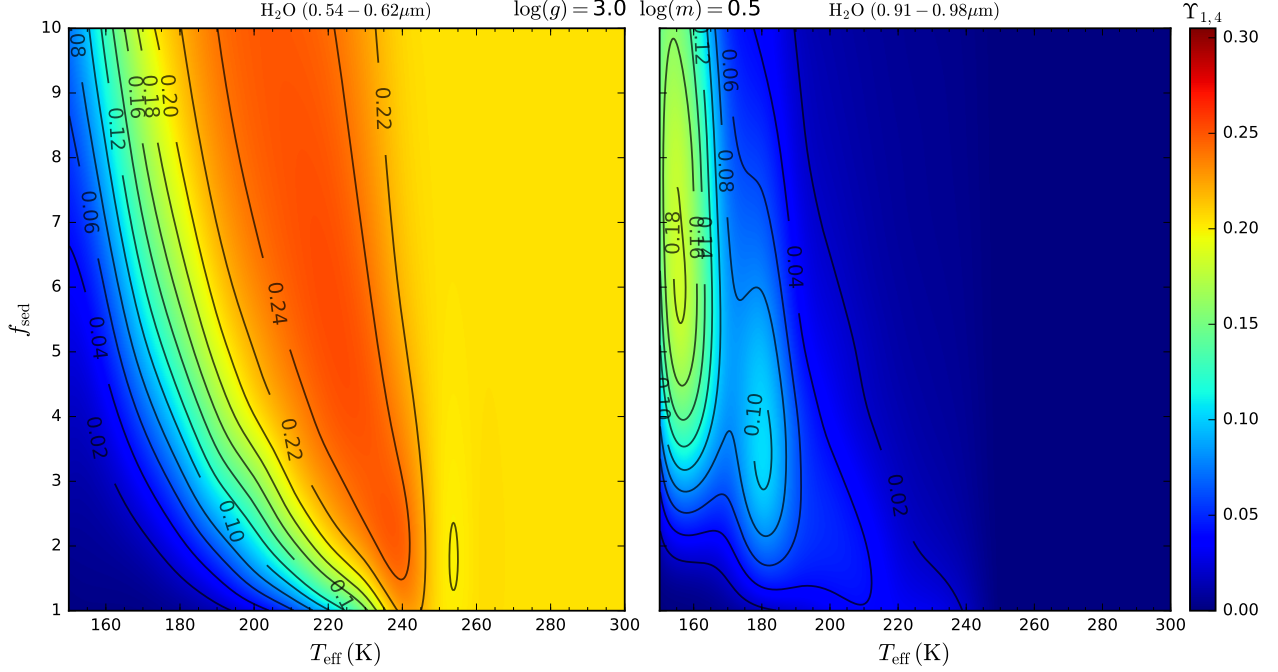


Figure 9. H₂O prominence in the $f_{\text{sed}} - T_{\text{eff}}$ plane. Left: H₂O absorption on the Rayleigh slope ($\sim 0.6 \mu\text{m}$). Right: H₂O absorption at the optical opacity maximum ($\sim 0.94 \mu\text{m}$). The colouring indicates the values of the spectral indices Υ_1 (left) and Υ_4 (right) – see section 4.1. The variation with g and m are shown in the animated figure, available in the HTML article.

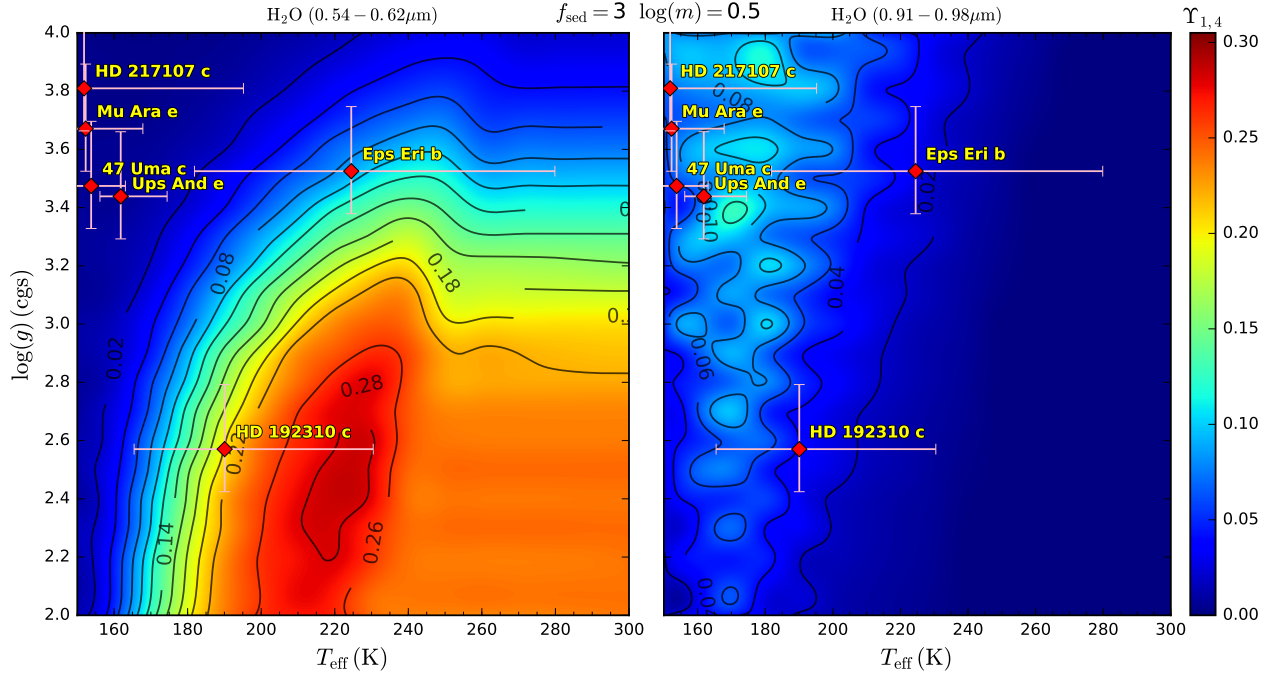


Figure 10. H₂O prominence in the $\log(g) - T_{\text{eff}}$ plane. Left: H₂O absorption on the Rayleigh slope ($\sim 0.6 \mu\text{m}$). Right: H₂O absorption at the optical opacity maximum ($\sim 0.94 \mu\text{m}$). The colouring indicates the values of the spectral indices Υ_1 (left) and Υ_4 (right) – see section 4.1. Approximate locations of known radial velocity exoplanets appropriate for direct imaging are shown. The value of g for each planet is obtained by assuming $M_p \sin(i) \sim M_p$ and inferring R_p using mass-radii relations (Fortney et al. 2007). An uncertainty in g of 40% is ascribed based on these assumptions. The T_{eff} values and uncertainties are derived from giant planet cooling models (Fortney et al. 2008), assuming a 100% error in the system age. The variation with f_{sed} and m are shown in the animated figure, available in the HTML article.

deep, optically thick, clouds to form. With these trends elu-

cidated, we now turn to examine how these insights can be utilised to inform future direct imaging observations.

5. IMPLICATIONS FOR OBSERVATIONS: H₂O VIA DIRECT IMAGING OF EXOPLANETS

Our exploration of parameter space in the previous section revealed that prominent H₂O signatures can exist in reflection spectra of cool giant planets. We shall now link our results to observations, identifying known radial velocity exoplanets amenable to detecting H₂O via direct imaging spectroscopy. We conclude by presenting self-consistent reflection spectra of the most promising target exoplanet.

5.1. Promising Exoplanets for Direct Imaging Spectroscopy

To place our results in the context of known exoplanets, we recast our H₂O prominence survey in the $\log(g) - T_{\text{eff}}$ plane, shown in Figure 10. Approximate locations of known radial velocity exoplanets suitable for direct imaging (Lupu et al. 2016) are overplotted. As the surface gravities have not been directly measured for these worlds, we infer them by assuming the measured $M_p \sin(i) \sim M_p$, and deriving R_p using theoretical mass-radii relations (Fortney et al. 2007). Given the crudeness of these assumptions, we ascribe a 40% error to each value of g . The values of T_{eff} for each planet are derived from giant planet cooling models (Fortney et al. 2008), with T_{eff} error bars accounting for a 100% error in the system age. As f_{sed} and m are not *a priori* determined, ‘Jupiter-like’ values of $f_{\text{sed}} = 3$ (Ackerman & Marley 2001) and $m = 3 \times$ solar (Wong et al. 2004) are presented in the static version of the figure, with the online animated version showing the variability with f_{sed} and $\log(m)$.

High gravity ($g \gtrsim 20 \text{ ms}^{-2}$) and low temperature ($T_{\text{eff}} \sim 160 \text{ K}$) planets are best observed around $0.94 \mu\text{m}$. As shown on the right of Figure 10, these conditions best apply to HD 217107 c, Mu Arae e, 47 Ursae Majoris c, and Upsilon Andromedae e. 55 Cancri d (not shown) is also an excellent target, with $T_{\text{eff}} \sim 150 \text{ K}$ and $g \sim 100 \text{ ms}^{-2}$ falling slightly above the maximum value of $\log(g)$ our models explored. These planets are predicted to possess especially prominent H₂O absorption for $f_{\text{sed}} \gtrsim 6$ and $m \lesssim 3 \times$ solar (Figure 10, animation). For higher values of m , the ‘H₂O island’ these planets reside on shifts to higher temperatures, which could result in Epsilon Eridani b (and possibly HD 192310 c) having detectable H₂O features for $m \gtrsim 10 \times$ solar.

Low gravity ($g \lesssim 20 \text{ ms}^{-2}$) planets are best observed at wavelengths $\lesssim 0.8 \mu\text{m}$. The left panel of Figure 10 demonstrates that the only target planet for which this currently applies is HD 192310 c. Such low gravity planets with $T_{\text{eff}} \gtrsim 180 \text{ K}$ are predicted to have Rayleigh slopes dominated by H₂O absorption, far exceeding the prominence of features around $0.94 \mu\text{m}$. Higher values of f_{sed} shift the ‘H₂O plateau’ to lower temperatures, improving the prospects of observing H₂O on cool, low gravity worlds – with $f_{\text{sed}} \gtrsim 7$ placing HD 192310 c inside the ‘cloud enhanced’ region of maximum H₂O prominence (Figure 10, animation). This effect could

also enable Epsilon Eridani b to have observable H₂O signatures at short wavelengths for $f_{\text{sed}} \gtrsim 5$. Both of these planets exhibit decreased H₂O prominence for $m \gtrsim 10 \times$ solar, as the regions of maximal prominence shift to higher temperatures. Interestingly, Epsilon Eridani b thus represents a case where H₂O features $\lesssim 0.8 \mu\text{m}$ are more prominent for high f_{sed} and low m , whilst features around $0.94 \mu\text{m}$ become more prominent for low f_{sed} and high m . Given that f_{sed} and m are not known for these planets, Epsilon Eridani b may thus represent a good target where simultaneous observations at both short and long wavelengths optimises the prospect of detecting H₂O. Guided by the picture offered by Figure 10, we proceed to examine self-consistent reflection spectra of HD 192310 c – the planet with the overall highest predicted H₂O prominence – in order to assess its potential for direct imaging spectroscopy.

5.2. Assessment of HD 192310 c

The HD 192310 (Gliese 785) system, located 8.82 pc from Earth, contains two known Neptune-mass exoplanets with semi-major axes of $0.32 \pm 0.005 \text{ AU}$ and $1.18 \pm 0.025 \text{ AU}$, respectively (Pepe et al. 2011). The outermost planet, HD 192310 c, has a slightly eccentric ($e = 0.32 \pm 0.11$) 526 ± 9 day orbit with an estimated equilibrium temperature of 185 K. Radial velocity observations with the HARPS instrument have measured $M_p \sin(i) = 24 \pm 5 M_{\oplus}$ ($0.076 \pm 0.016 M_J$) (Pepe et al. 2011). These system parameters place HD 192310 c near the currently proposed inner working angle of WFIRST (Nayak et al. 2017), making direct imaging observations of this planet challenging but not impossible.

In order to model geometric albedo spectra of this planet, some assumptions must be made. Given the unknown radius, we use the mass-radii relations of Fortney et al. (2007) to infer $R_p \approx 0.71 R_J$. Taking $M_p \sin(i) = M_p$, we derive a surface gravity of $g = 3.72 \text{ ms}^{-2}$. Using a planetary evolution model (Fortney et al. 2008), we find $T_{\text{eff}} = 190_{-25}^{+40} \text{ K}$. A reasonable value of $f_{\text{sed}} = 3$ is chosen. Unlike our models in previous sections, here we use P-T profiles that self-consistently include the effect of clouds via coupling to the Ackerman & Marley (2001) cloud model. Atmospheres with five different metallicities are considered: $\log(m) = 0.0, 0.5, 1.0, 1.5,$ and $1.7 \times$ solar (corresponding to $m = 1, 3.16, 10, 31.6,$ and $50 \times$ solar). The resulting geometric albedo spectra, previously shown in Nayak et al. (2017), and P-T profiles for the solar, $10 \times$ solar, and $50 \times$ solar models are presented in Figure 11.

Our self-consistent models of HD 192310 c confirm that H₂O absorption can play a prominent role in shaping its geometric albedo spectrum. In particular, the prediction from Sections 3 and 4 that planets with $g \lesssim 20 \text{ ms}^{-2}$ should display significant H₂O signatures at wavelengths $\lesssim 0.8 \mu\text{m}$ is vindicated. We also see that the predicted trend of $m \gtrsim 10 \times$ solar brightening the continuum albedo, but resulting in severely

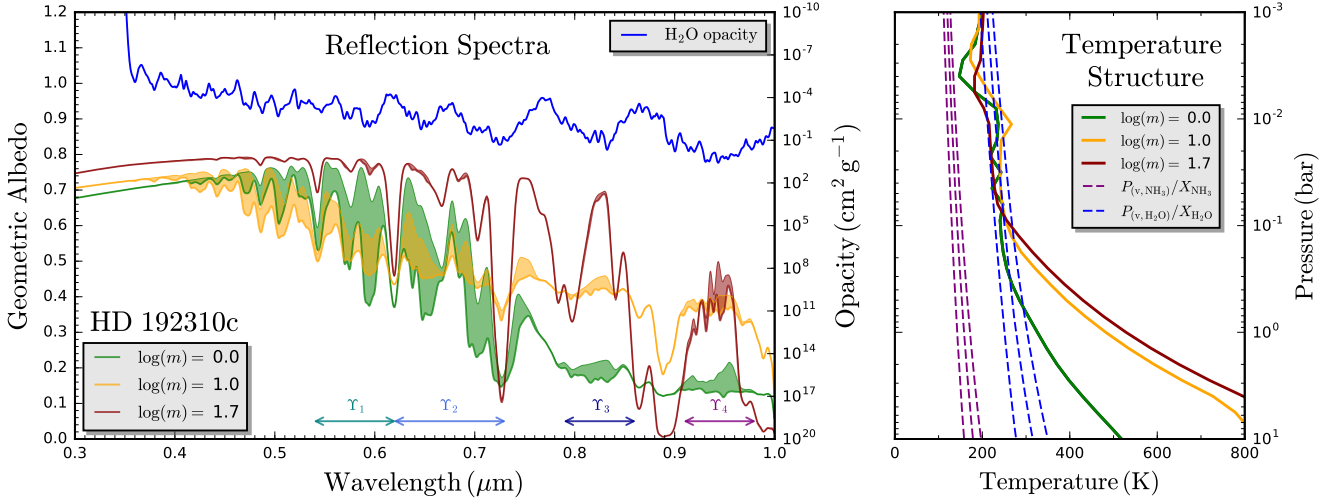


Figure 11. Self-consistent reflection spectra and P-T profiles for HD 192310c. Left: geometric albedo spectra for three models of HD 192310 c’s atmosphere: $m = 1 \times$ solar (green), $m = 10 \times$ solar (orange), and $m = 50 \times$ solar (red). Two curves are plotted for each model; the lower curve has H₂O opacity enabled, the upper has H₂O opacity disabled, with the enclosed shading indicating absorption due to H₂O. All models assume $T_{\text{eff}} = 190$ K, $f_{\text{sed}} = 3$, and $g = 3.72 \text{ ms}^{-2}$. The H₂O opacity is shown in blue (smoothed for clarity). Right: P-T profiles corresponding to the same three models, with the NH₃ (purple) and H₂O (blue) condensation curves for each value of m (increasing from left to right).

dampened short wavelength H₂O signatures (e.g. Figure 7), holds for the self-consistent models. We note that the self-consistent models do exhibit one additional feature, namely that the presence of multiple cloud decks can be caused by high-altitude thermal inversions. Such an effect was not encountered in our parameter space exploration, as our parametric P-T profile (Section 2.3.1) has a temperature structure that monotonically decreases with altitude. However, this does not overly modify our earlier conclusions, as these high-altitude cloud decks tend to be optically thin.

The prominence of H₂O absorption and key cloud properties for each of our HD 192310 c atmosphere models are summarised in Table 1. H₂O prominence is expressed in terms of the spectral indices $\Upsilon_{1,2,3,4}$ (Section 4.1), with clouds summarised by the cloud base pressure, P_{base} , cloud deck thickness, ΔP_{cloud} , and the maximum layer optical depth within each cloud deck, $\tau_{\text{cloud,max}}$. The asymmetry parameter and single scattering albedo are essentially the same for all H₂O clouds ($\bar{g} \approx 0.89$, $\bar{\omega} \approx 0.999$). Comparing with Figure 10, our parameter space survey predicted $\Upsilon_1 \approx 0.22$ for $\log(m) = 0.5 \times$ solar, which matches well with the self-consistent value of 0.173. Our predicted value of $\Upsilon_4 \approx 0.04$ agrees with the higher metallicity models, but under-predicts the prominence of H₂O at $0.94 \mu\text{m}$ yielded by the self-consistent model (0.123). This is caused by brightening by the sudden transition to an optically thick H₂O cloud deck when m first increases to $\sim 3 \times$ solar – due to the H₂O condensation curve shifting to higher temperatures, resulting in a deeper intersection point.

Table 1. Theoretical H₂O Prominence and Cloud Properties for HD 192310 c

$\log(m)$ (\times solar)	Υ_1^a	Υ_2	Υ_3	Υ_4	P_{base} (mbar)	$\Delta P_{\text{cloud}}^b$ (mbar)	$\tau_{\text{cloud,max}}$
0.0	0.300	0.227	0.020	0.019	16	12	0.7
0.5	0.173	0.137	0.037	0.123	4 / 251 ^c	2 / 162	0.7 / 13
1.0	0.145	0.097	0.025	0.035	8 / 126	5 / 63	5.2 / 3.6
1.5	0.011	0.018	0.016	0.054	8 / 251	4 / 206	0.6 / 239
1.7	0.009	0.014	0.009	0.040	11 / 251	5 / 229	0.7 / 304

^a Spectral indices Υ_i , as defined by Equation 9.

^b Thickness of cloud deck(s) above cloud base.

^c Slashes (/) indicate multiple cloud decks.

The models with $\log m \geq 0.5 \times$ solar also exhibit secondary high altitude cloud decks at $\sim 1 - 10$ mbar. These are a consequence of weak thermal inversions in the upper atmosphere, leading to multiple crossings of the relevant H₂O condensation curves. This does not occur for the solar metallicity model, which only intersects the condensation curve once at 16 mbar. These secondary cloud decks are optically thin in most cases, with the one exception being our $\log m = 1.0 \times$ solar model, for which the two cloud decks have similar optical depths. As shown in Figure 11, two distinct, moderately scattering, cloud decks still yield especially prominent H₂O features for $\lambda \lesssim 0.7 \mu\text{m}$. These H₂O signatures in particular underscore the importance of low g planets to observations.

6. SUMMARY AND DISCUSSION

We have conducted an extensive parameter space survey to assess the prominence of H₂O absorption signatures in reflection spectra of cool giant exoplanets. We have quantitatively explored the impact of effective temperature, gravity, sedimentation efficiency, and metallicity, providing > 50,000 reflection spectra models for the community². Our main conclusions are as follows:

- Giant planets $\gtrsim 30$ K warmer than Jupiter can exhibit reflection spectra substantially altered by H₂O.
- Prominent H₂O absorption features exist from $\sim 0.91 - 0.98 \mu\text{m}$, $\sim 0.79 - 0.86 \mu\text{m}$, and are embedded in the Rayleigh slope from $\sim 0.4 - 0.73 \mu\text{m}$.
- Planets with $g \lesssim 20 \text{ ms}^{-2}$ and $T_{\text{eff}} \gtrsim 180$ K exhibit the most prominent H₂O features, manifestly observable at short wavelengths $\lesssim 0.7 \mu\text{m}$. This holds across a wide range of possible values for m and f_{sed} .
- Planets with $g \gtrsim 20 \text{ ms}^{-2}$ and $T_{\text{eff}} \sim 150$ K can exhibit notable H₂O features around $0.94 \mu\text{m}$, given $f_{\text{sed}} \gtrsim 3$ and $m \lesssim 10 \times$ solar.
- Higher f_{sed} enables lower temperature planets to support prominent H₂O features.
- Higher m tends to weaken H₂O features, resulting in bright planets dominated by scattering H₂O clouds.
- HD 192310 c is identified as the most promising currently known cool giant planet to detect H₂O via direct imaging in reflected light.

Of all our results, we draw particular attention to the finding that low gravity planets possess exceptionally strong H₂O features along the Rayleigh slope from $\sim 0.4 - 0.73 \mu\text{m}$. To our knowledge, observable H₂O features at such short wavelengths have not previously been discussed in the literature, so our finding that they are often the most potent H₂O signatures bears note. The enhanced presence of such features for low gravity planets is due to the combination of optically thin clouds and large density scale heights – resulting in long path lengths for relatively cloud-free atmospheres. On the other hand, the $0.94 \mu\text{m}$ H₂O feature cannot rely on a Rayleigh scattering continuum, and so is less prominent despite possessing a H₂O opacity exceeding that at shorter wavelengths by orders of magnitude. Indeed, the $0.94 \mu\text{m}$ feature critically depends on clouds to brighten the albedo at these wavelengths, which results in narrow regions of parameter space where it may be observed. Conversely, the $\sim 0.4 - 0.73 \mu\text{m}$

H₂O features need only require a relatively cloud-free low gravity planet to be prominent, which holds true over a vast expanse of parameter space.

We have explicitly highlighted, via self-consistent modelling of HD 192310 c, the substantial imprint of H₂O in a low gravity planet’s reflection spectrum. As this is the only known radial velocity planet amenable to direct imaging with an estimated $g \lesssim 20 \text{ ms}^{-2}$, there is an urgent need to identify additional Neptune-mass exoplanets with $T_{\text{eff}} \gtrsim 180$ K to capitalise on ‘gravity enhanced’ H₂O signatures.

Our results demonstrate a profound advantage for spectroscopic observations at short wavelengths from $\sim 0.4 - 0.73 \mu\text{m}$. WFIRST spectroscopy, by comparison, is envisioned to have a minimum observable wavelength of $0.6 \mu\text{m}$ (Spiegel et al. 2015), resulting in a narrow range where gravity enhanced H₂O signatures can be harnessed. Future direct imaging missions, such as LUVOIR or HabEx, should aim for the greatest flexibility to obtain spectra over large ranges of λ/D , where D is telescope diameter, to maintain the ability to fully exploit this effect for a large variety of planets.

Interpretations of direct imaging observations will additionally have to contend with effects not considered here. Observational constraints will necessitate imaging at larger phase angles than the zero phase angle geometric albedo spectra we have examined – typically between $40 - 130^\circ$ for edge-on systems with WFIRST (Mayorga et al. 2016). Under the typical observing condition of quarter-phase, partial illumination can result in reflection spectra darker by a factor of 3-4 around $0.55 \mu\text{m}$ and $0.75 \mu\text{m}$ (Sudarsky et al. 2005; Mayorga et al. 2016). Inferences of H₂O features $\lesssim 0.5 \mu\text{m}$ will additionally require modelling of photochemical hazes, which can substantially darken short wavelength albedo spectra (Marley et al. 1999; Sudarsky et al. 2000; Gao et al. 2017). Furthermore, our modelling framework explicitly assumes abundances of non-condensing species are governed by thermochemical equilibrium. The atmospheres of both Jupiter and Saturn contain disequilibrium gasses (e.g., PH₃) delivered to the observable atmosphere by vertical mixing (Atreya et al. 1999), whilst evidence of disequilibrium chemistry from exoplanet atmospheric retrievals has recently emerged from studies of exo-Neptunes (Morley et al. 2017), directly imaged planets (Lavie et al. 2017), and hot Jupiters (MacDonald & Madhusudhan 2017). We thus should not be surprised if the atmospheres of cool giant exoplanets are not in chemical equilibrium.

Beyond detecting H₂O, our results suggest that it may be possible to infer the mixing ratio of H₂O from atmospheric retrievals of reflection spectra. The prominence of H₂O signatures can rival that of CH₄, particularly for low gravity planets, and so abundance constraints could be derived from low-resolution observations similar to that expected of WFIRST ($R \approx 50$). Atmospheric retrieval tech-

² Reflection Spectra Repository

niques for reflection spectra have seen development in recent years (Barstow et al. 2014; Lupu et al. 2016; Nayak et al. 2017; Lacy et al. 2018), but much of this work has focused on CH₄ as the dominant molecular opacity source. Our present study demonstrates the need to include H₂O vapour as a parameter in reflection spectra retrievals. Indeed, the sensitivity of H₂O features to the value of g offers a potential solution to the issue whereby g is poorly constrained when retrieving CH₄ alone (Lupu et al. 2016). Ultimately, the application of such retrieval methods offers the prospect of deriving constraints on the C/O, O/H, and other elemental ratios for cool giant planets. Such elemental ratios, constrained across a wide sample of extrasolar Jupiter analogues, offers extraordinary promise for resolving outstanding questions on the formation mechanisms for cool giant planets.

The opportunity to conduct this research was enabled by the 2016 Kavli Summer Program in Astrophysics, supported by grants from The Kavli Foundation, The National Science Foundation, UC Santa Cruz, and UCSC’s Other Worlds Laboratory. In particular, we commend P. Garaud, the program coordinator, and the Scientific Organising Committee (J. Fortney, D. Abbot, C. Goldblatt, R. Murray-Clay, D. Lin, A. Showman and X. Zhang). R.J.M. additionally acknowledges financial support from the Science and Technology Facilities Council (STFC), UK, toward his doctoral program. We thank P. Gao for insightful discussions on geometric albedo spectra.

APPENDIX

A. A PRESSURE-TEMPERATURE PROFILE FOR COOL GIANT PLANETS

Here we describe the origin of the P-T profiles employed in our cool giant planet model grid. Our aim was to develop a simple empirical fitting function capable of approximately reproducing the temperature structure of cool giant planets under radiative-convective equilibrium, thereby circumventing the computational cost of running thousands of equilibrium models directly.

We began with a set of 68 self-consistent P-T profile models computed using the methods described in Fortney et al. (2008). These profiles model giant planets around a solar-analogue with g from 10 ms⁻² to 100 ms⁻², m from 1× to 100× solar, and a from 0.5 AU to 5.0 AU. All models have $T_{\text{int}} = 150$ K, C/O = 0.5, and assume a cloud-free atmosphere under radiative-convective equilibrium. The model atmospheres are divided into 60 layers, specified at 61 depth points uniformly spaced in log-P from 10⁻⁶ bar to 10³ bar. T_{eff} was derived for each model from integrating the thermal emission. Each model is thus specified by g , $\log(m)$, and a (or T_{eff}). The parameters describing each of the models used are given in Table A.

For each of these self-consistent P-T profile models, we fit a simple two-parameter function:

$$T^4(P) = T_0^4 + T_{\text{deep}}^4 (P/1000\text{bar}) \quad (4)$$

where T is the atmospheric temperature at pressure P (in bar), and the free parameters are T_0 and T_{deep} . This functional form is essentially just the Eddington relation with negligible irradiation ($T_{\text{irr}} \ll T_{\text{int}}$), with the grey optical depth, τ , taken to be proportional to P and with the various constants absorbed into the parameters T_0 and T_{deep} . Physically, T_0 and T_{deep} encode the temperatures of an upper-atmosphere isotherm and the temperature at the 1000 bar level.

We derived best-fitting values of the parameters T_0 and T_{deep} using a technique borrowed from exoplanet atmospheric retrieval. For a given self-consistent model, the temperature in each layer, $T_{\text{Fortney}}(P_i)$, can be taken as a ‘data-point’. For a given point in the T_0 - T_{deep} plane, a ‘model’ temperature profile, $T_{\text{fit}}(P_i)$, can be constructed using Equation 4. By comparing the ‘data’ to the ‘model’, a likelihood function can be constructed:

$$\log \mathcal{L} = \sum_{i=1}^N -\frac{[T_{\text{Fortney}}(P_i) - T_{\text{fit}}(T_0, T_{\text{deep}}, P_i)]^2}{2\delta_T^2} \quad (\text{A.1})$$

where N is the number of depth points (61), and δ_T is an arbitrary ‘temperature tolerance’ factor that encodes an ‘error’ in the self-consistent model temperatures. This functional form essentially assumes independently distributed Gaussian ‘errors’, with an additive normalisation factor in the log-likelihood neglected (due to it being identical for all sampled values of T_0 and T_{deep}). For our purposes, where we essentially assume the self-consistent models represent ‘ground truth’, we take $\delta_T = 1$ K (smaller values increase the fitting time, with negligible influence on the final derived fits). We employ the MultiNest algorithm (Feroz & Hobson 2008; Feroz et al. 2009) to map the T_0 and T_{deep} plane, bounded by wide uniform priors from 0 K to 1000 K for T_0 and 600 K to 3000 K for T_{deep} . We ran MultiNest once for each self-consistent profile (typically involving $\sim 10^5$ likelihood evaluations), drawing the maximum likelihood posterior sample values of T_0 and T_{deep} to arrive at the optimal fitted profile.

We compare the fitted profile using Equation 4 to the self-consistent input profiles for six models in Figure A. The plotted models are for a solar metallicity Jupiter analogue ($g = 25$ ms⁻²) with semi-major axes from 0.5 AU to 4.0 AU. The five models

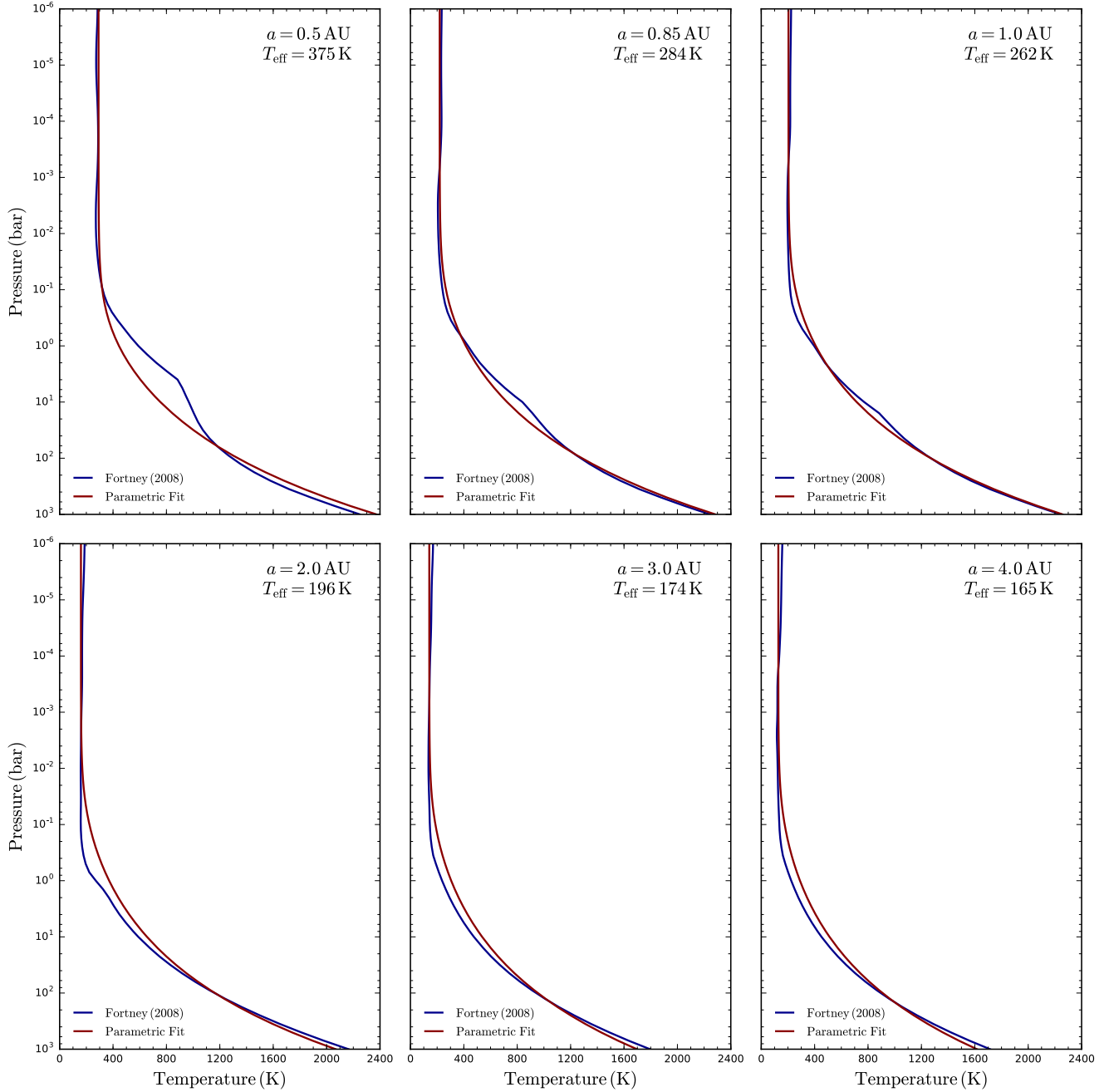


Figure A. Comparison between self-consistent cool giant planet P-T profiles (Fortney et al. 2008) (blue) and the best-fitting P-T profiles described by Equation 4 (red). The six profiles are for a solar metallicity cloud-free Jovian analogue ($g = 25 \text{ ms}^{-2}$) with $T_{\text{int}} = 150 \text{ K}$, and $\text{C/O} = 0.5$, with planet-star separations from 0.5 to 4.0 AU. The values of T_{eff} corresponding to each model are given in the top right of each panel.

with $T_{\text{eff}} < 300 \text{ K}$ are generally well-fit, with maximum deviations between the self-consistent P-T profile and the fitted profile $< 120 \text{ K}$ (with mean deviations $< 40 \text{ K}$). Discrepancies grow for models with $T_{\text{eff}} > 300 \text{ K}$, as shown in the upper left panel of Figure A, due to the parametrisation of Equation 4 being unable to account for the influence of non-negligible external radiation. For this case ($a = 0.5 \text{ AU}$), the maximum deviation between the self-consistent P-T profile and the fitted profile is 280 K (with a mean deviations of 60 K). We thus note that the maximum effective temperature over which our cool giant planet P-T profile fits should be utilised is $\sim 300 \text{ K}$ (it is for this reason that Figures 9 and 10 do not go above 300 K). Similarly, our profile should not be used for $T_{\text{eff}} < 150 \text{ K}$, as T_{eff} cannot be less than T_{int} (150 K for all the input self-consistent profiles).

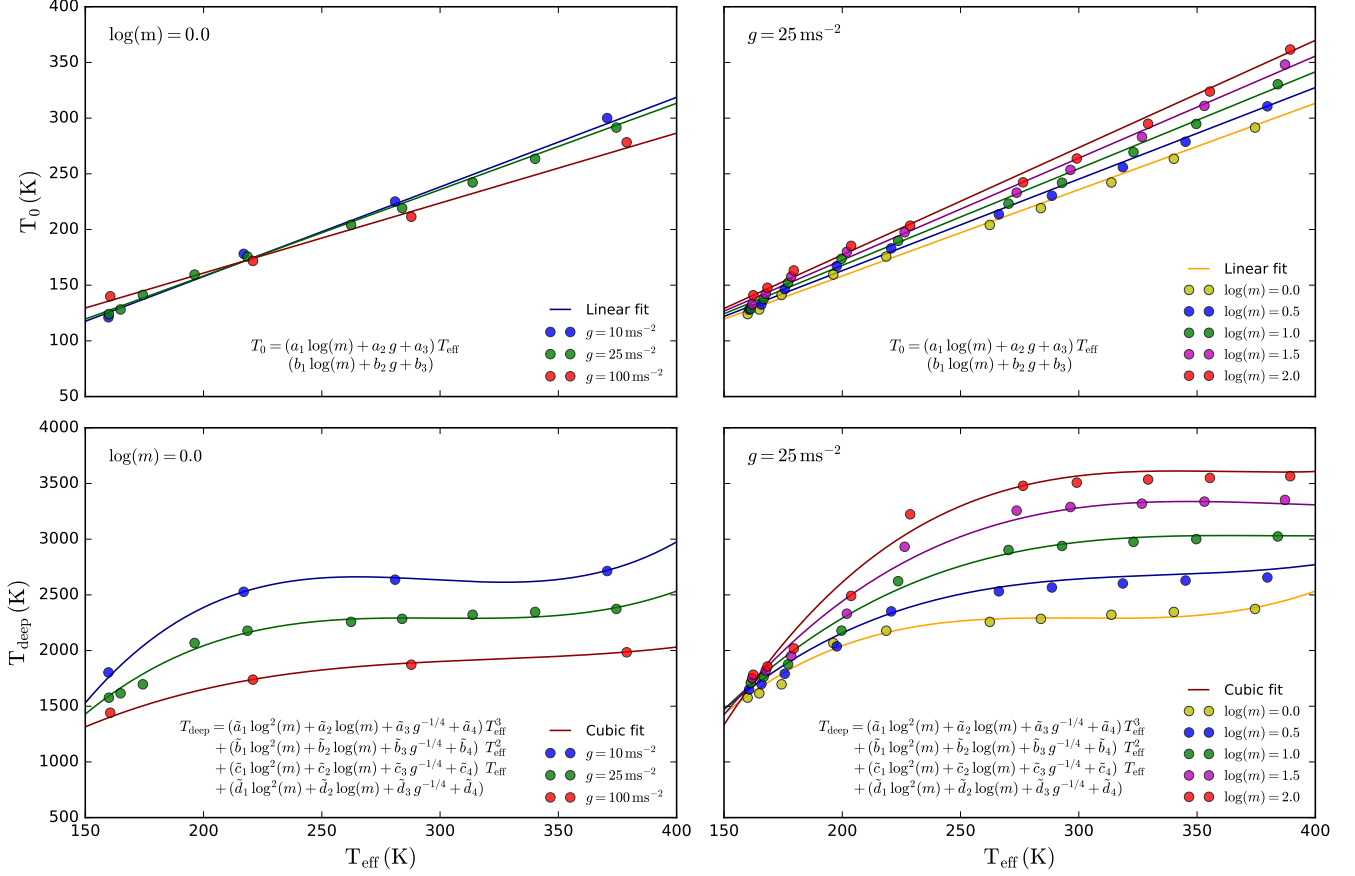


Figure B. Variation of the best-fitting values of T_0 and T_{deep} with metallicity, gravity, and effective temperature. Left: variation with g and T_{eff} for fixed m . Right: variation with m and T_{eff} for fixed g . The points show the values of T_0 and T_{deep} that maximise Equation A.1 for each of the self-consistent models in Table A. The curves are fitting functions to the points, expressed in Equations A.2 and A.3 (numerical values of the expansion coefficients are given in the text).

The best-fitting values of T_0 and T_{deep} for each of the 68 self-consistent P-T profiles are plotted as functions of T_{eff} in Figure B. We investigated a number of functional forms for $T_0(\log(m), g, T_{\text{eff}})$ and $T_{\text{deep}}(\log(m), g, T_{\text{eff}})$ able to reproduce the broad trends in these quantities across parameter space. Least-squares fitting for each functional form was conducted for fixed m to derive fitting coefficients for variations in g and for fixed g to derive coefficients for variations in m . Coefficients were matched at the common intersection point of these two families of solutions ($g = 25 \text{ ms}^{-2}$ and $\log(m) = 0.0$).

For T_0 , a linear relation with T_{eff} was found to be adequate, taking the form:

$$T_0 = (a_1 \log(m) + a_2 g + a_3) T_{\text{eff}} + (b_1 \log(m) + b_2 g + b_3) \quad (\text{A.2})$$

where $a_1 = 0.0939629520975$, $a_2 = -0.00195955723764$, $a_3 = 0.824004813287$, $b_1 = -9.3354717917$, $b_2 = 0.426544316687$, and $b_3 = -7.35793593873$. For T_{deep} , the minimal order polynomial fitting function was found to be cubic in T_{eff} :

$$T_{\text{deep}} = (\tilde{a}_1 \log^2(m) + \tilde{a}_2 \log(m) + \tilde{a}_3 g^{-1/4} + \tilde{a}_4) T_{\text{eff}}^3 + (\tilde{b}_1 \log^2(m) + \tilde{b}_2 \log(m) + \tilde{b}_3 g^{-1/4} + \tilde{b}_4) T_{\text{eff}}^2 + (\tilde{c}_1 \log^2(m) + \tilde{c}_2 \log(m) + \tilde{c}_3 g^{-1/4} + \tilde{c}_4) T_{\text{eff}} + (\tilde{d}_1 \log^2(m) + \tilde{d}_2 \log(m) + \tilde{d}_3 g^{-1/4} + \tilde{d}_4) \quad (\text{A.3})$$

where $\tilde{a}_1 = 0.000122391650778$, $\tilde{a}_2 = -0.000253005417439$, $\tilde{a}_3 = 0.00130682904558$, $\tilde{a}_4 = -0.000324145003492$, $\tilde{b}_1 = -0.101884473342$, $\tilde{b}_2 = 0.188364010495$, $\tilde{b}_3 = -1.1319726177$, $\tilde{b}_4 = 0.271721883808$, $\tilde{c}_1 = 26.8759214447$, $\tilde{c}_2 = -40.9475604372$, $\tilde{c}_3 = 317.541624812$, $\tilde{c}_4 = -71.729686904$, $\tilde{d}_1 = -2241.35380397$, $\tilde{d}_2 = 2888.7627511$, $\tilde{d}_3 = -25698.9658072$, $\tilde{d}_4 = 6778.41758375$.

For given values of $\log(m)$, g , and T_{eff} , substitution into Equations A.2 and A.3 yield T_0 and T_{deep} . Substituting these into Equation 4 then yields an a priori determined P-T profile valid for cool giant planets with T_{eff} in the range ~ 150 -300 K.

Table A. Fortney et al. (2008) P-T models employed during parametric fitting of Equation 4.

g (ms^{-2})	$\log(m)$ (\times solar)	a (AU)
10	0.0	0.5, 0.85, 1.5, 5.0
25	0.0, 0.5, 1.0 1.5, 1.7, 2.0	0.5, 0.6, 0.7, 0.85, 1.0 1.5, 2.0, 3.0, 4.0, 5.0
100	0.0	0.5, 0.85, 1.5, 5.0

REFERENCES

- Ackerman, A. S., & Marley, M. S. 2001, *ApJ*, 556, 872
- Atreya, S. K., Wong, M. H., Owen, T. C., et al. 1999, *Planet. Space Sci.*, 47, 1243
- Barman, T. S., Konopacky, Q. M., Macintosh, B., & Marois, C. 2015, *ApJ*, 804, 61
- Barstow, J. K., Aigrain, S., Irwin, P. G. J., et al. 2014, *ApJ*, 786, 154
- Benneke, B. 2015, ArXiv e-prints, arXiv:1504.07655
- Bolcar, M. R., Feinberg, L., France, K., et al. 2016, in *Proc. SPIE*, Vol. 9904, *Space Telescopes and Instrumentation 2016: Optical, Infrared, and Millimeter Wave*, 99040J
- Bolton, S. J. 2010, in *IAU Symposium*, Vol. 269, *Galileo's Medicean Moons: Their Impact on 400 Years of Discovery*, ed. C. Barbieri, S. Chakrabarti, M. Coradini, & M. Lazzarin, 92–100
- Buck, A. L. 1981, *J. Appl. Meteorol.*, 20, 1527
- Burrows, A. 2014, ArXiv e-prints, arXiv:1412.6097
- Burrows, A., Sudarsky, D., & Hubeny, I. 2004, *ApJ*, 609, 407
- Burrows, A., Marley, M., Hubbard, W. B., et al. 1997, *ApJ*, 491, 856
- Cahoy, K. L., Marley, M. S., & Fortney, J. J. 2010, *ApJ*, 724, 189
- Chamberlain, J. W., & Hunten, D. M. 1987, *Orlando FL Academic Press Inc International Geophysics Series*, 36
- Deming, D., Wilkins, A., McCullough, P., et al. 2013, *ApJ*, 774, 95
- Ehrenreich, D., Bonfils, X., Lovis, C., et al. 2014, *Astron. Astrophys.*, 570, A89
- Evans, T. M., Sing, D. K., Kataria, T., et al. 2017, *Nature*, 548, 58
- Feroz, F., & Hobson, M. P. 2008, *Mon. Not. R. Astron. Soc.*, 384, 449
- Feroz, F., Hobson, M. P., & Bridges, M. 2009, *Mon. Not. R. Astron. Soc.*, 398, 1601
- Fortney, J. J. 2005, *MNRAS*, 364, 649
- Fortney, J. J., Lodders, K., Marley, M. S., & Freedman, R. S. 2008, *ApJ*, 678, 1419
- Fortney, J. J., Marley, M. S., & Barnes, J. W. 2007, *ApJ*, 659, 1661
- Fortney, J. J., Marley, M. S., Saumon, D., & Lodders, K. 2008, *ApJ*, 683, 1104
- Fraine, J., Deming, D., Benneke, B., et al. 2014, *Nature*, 513, 526
- Freedman, R. S., Marley, M. S., & Lodders, K. 2008, *Astrophys. J. Suppl. Ser.*, 174, 504
- Gao, P., Marley, M. S., Zahnle, K., Robinson, T. D., & Lewis, N. K. 2017, *AJ*, 153, 139
- Gierasch, P. J., & Conrath, B. J. 1985, *Energy conversion processes in the outer planets* (Cambridge and New York: Cambridge University Press), 121–146
- Karkoschka, E. 1994, *Icarus*, 111, 174
- . 1998, *Icarus*, 133, 134
- Knutson, H. A., Benneke, B., Deming, D., & Homeier, D. 2014, *Nature*, 505, 66
- Konopacky, Q. M., Barman, T. S., Macintosh, B. A., & Marois, C. 2013, *Science*, 339, 1398
- Kreidberg, L., Bean, J. L., Désert, J.-M., et al. 2014a, *Nature*, 505, 69
- Kreidberg, L., Bean, J. L., Désert, J.-M., et al. 2014b, *The Astrophysical Journal Letters*, 793, L27
- Lacy, B., Shlivko, D., & Burrows, A. 2018, ArXiv e-prints, arXiv:1801.08964
- Lavie, B., Mendonça, J. M., Mordasini, C., et al. 2017, *AJ*, 154, 91
- Lewis, J. S. 1969, *Icarus*, 10, 365
- Lindal, G. F., Wood, G. E., Levy, G. S., et al. 1981, *J. Geophys. Res. Sp. Phys.*, 86, 8721
- Line, M. R., Wolf, A. S., Zhang, X., et al. 2013, *ApJ*, 775, 137
- Lupu, R. E., Marley, M. S., Lewis, N., et al. 2016, *AJ*, 152, 217
- MacDonald, R. J., & Madhusudhan, N. 2017, *ApJL*, 850, L15
- Macintosh, B., Graham, J. R., Barman, T., et al. 2015, *Science*, 350, 64
- Madhusudhan, N., Agúndez, M., Moses, J. I., & Hu, Y. 2016, *Space Sci. Rev.*, 1

- Madhusudhan, N., Crouzet, N., McCullough, P. R., Deming, D., & Hedges, C. 2014, *ApJL*, 791, L9
- Madhusudhan, N., & Seager, S. 2009, *ApJ*, 707, 24
- Marley, M. 2000, in *Astronomical Society of the Pacific Conference Series*, Vol. 212, *From Giant Planets to Cool Stars*, ed. C. A. Griffith & M. S. Marley, 152
- Marley, M. S., Gelino, C., Stephens, D., Lunine, J. I., & Freedman, R. 1999, *ApJ*, 513, 879
- Marley, M. S., & McKay, C. P. 1999, *Icarus*, 138, 268
- Marley, M. S., Saumon, D., Guillot, T., et al. 1996, *Science*, 272, 1919
- Marley, M. S., Seager, S., Saumon, D., et al. 2002, *ApJ*, 568, 335
- Martonchik, J. V., Orton, G. S., & Appleby, J. F. 1984, *Appl. Opt.*, 23, 541
- Mayorga, L. C., Jackiewicz, J., Rages, K., et al. 2016, *AJ*, 152, 209
- McKay, C. P., Pollack, J. B., & Courtin, R. 1989a, *Icarus*, 80, 23
— 1989b, *Icarus*, 80, 23
- Mennesson, B., Gaudi, S., Seager, S., et al. 2016, in *Proc. SPIE*, Vol. 9904, *Space Telescopes and Instrumentation 2016: Optical, Infrared, and Millimeter Wave*, 99040L
- Morley, C. V., Fortney, J. J., Marley, M. S., et al. 2012, *ApJ*, 756, 172
— 2015, *ApJ*, 815, 22
- Morley, C. V., Knutson, H., Line, M., et al. 2017, *AJ*, 153, 86
- Morley, C. V., Marley, M. S., Fortney, J. J., et al. 2014, *ApJ*, 787, 21
- Mousis, O., Lunine, J. I., Madhusudhan, N., & Johnson, T. V. 2012, *ApJL*, 751, L7
- Nayak, M., Lupu, R., Marley, M. S., et al. 2017, *PASP*, 129, 034401
- Öberg, K. I., Murray-Clay, R., & Bergin, E. A. 2011, *ApJL*, 743, L16
- Pepe, F., Lovis, C., Ségransan, D., et al. 2011, *Astron. Astrophys.*, 534, A58
- Richard, C., Gordon, I., Rothman, L., et al. 2012, *J. Quant. Spectrosc. Radiat. Transf.*, 113, 1276
- Saumon, D., & Marley, M. S. 2008, *ApJ*, 689, 1327
- Saumon, D., Marley, M. S., Abel, M., Frommhold, L., & Freedman, R. S. 2012, *ApJ*, 750, 74
- Seager, S. 2010, *Exoplanet Atmospheres: Physical Processes* (Princeton University Press)
- Sedaghati, E., Boffin, H. M. J., MacDonald, R. J., et al. 2017, *Nature*, 549, 238
- Sing, D. K., Fortney, J. J., Nikolov, N., et al. 2016, *Nature*, 529, 59
- Snellen, I. A. G., Albrecht, S., de Mooij, E. J. W., & Poole, R. S. L. 2008, *Astron. Astrophys.*, 487, 357
- Snellen, I. A. G., de Kok, R. J., de Mooij, E. J. W., & Albrecht, S. 2010, *Nature*, 465, 1049
- Spergel, D., Gehrels, N., Baltay, C., et al. 2015, *ArXiv e-prints*, arXiv:1503.03757
- Stephens, D. C., Leggett, S. K., Cushing, M. C., et al. 2009, *ApJ*, 702, 154
- Sudarsky, D., Burrows, A., Hubeny, I., & Li, A. 2005, *ApJ*, 627, 520
- Sudarsky, D., Burrows, A., & Pinto, P. 2000, *ApJ*, 538, 885
- Toon, O. B., B. Pollack, J., & Sagan, C. 1977, *Icarus*, 30, 663
- Toon, O. B., McKay, C. P., Ackerman, T. P., & Santhanam, K. 1989, *J. Geophys. Res.*, 94, 16287
- van Dishoeck, E. F., Bergin, E. A., Lis, D. C., & Lunine, J. I. 2014, *Protostars and Planets VI*, 835
- Wakeford, H. R., Sing, D. K., Kataria, T., et al. 2017, *Science*, 356, 628
- Warren, S. G. 1984, *Appl. Opt.*, 23, 1206
- Wilson, P. A., Sing, D. K., Nikolov, N., et al. 2015, *MNRAS*, 450, 192
- Wong, M. H., Mahaffy, P. R., Atreya, S. K., Niemann, H. B., & Owen, T. C. 2004, *Icarus*, 171, 153
- Yurchenko, S. N., Barber, R. J., & Tennyson, J. 2011, *MNRAS*, 413, 1828